Low Reynolds number gravitational settling of a sphere through a fluid-fluid interface: Modelling using a boundary integral method

Paul Jarvis[*1], Jon Blundy[1], Katharine Cashman[1], Herbert E Huppert[1,2], and Heidy Mader[1]

[1]School of Earth Sciences, University of Bristol, Wills Memorial Building, Queens Road, Bristol, BS8 1RJ, UK

[2]Department of Applied Mathematics and Theoretical Physics, University of Cambridge, Wilberforce Road, Cambridge, CB3 0WA, UK

Abstract

1   Introduction

2   Fundamentals of Stokes Flow

We present here a background to the fundamentals of Stokes flow, covering the equations of motion and non-dimensionalisation, different types of boundary condition, Greens functions and the integral representation of Stokes flow. Throughout this document we will

---

[*]Corresponding author:paul.jarvis@bristol.co.uk

be making use of the Einstein summation convention and tensor notation (Riley et al., 2006).

2.1   Equations of Motion

The starting points for the majority of fluid dynamical problems are the continuity (equation 1) and Navier Stokes (equation 2) equations (Batchelor, 1967). Defining the fluid density ρ, the dynamic viscosity η, the fluid velocity field u_i and the pressure field P these are expressed as

$$\frac{\partial \rho(\boldsymbol{x}, t)}{\partial t} + \partial_i[\rho(\boldsymbol{x}, t) u_i(\boldsymbol{x}, t)] = 0, \tag{1}$$

and

$$\left(\frac{\partial [u_i(\boldsymbol{x}, t) \rho(\boldsymbol{x}, t)]}{\partial t} + [u_j(\boldsymbol{x}, t) \partial_j][u_i(\boldsymbol{x}, t) \rho(\boldsymbol{x}, t)] \right) = -\partial_i P(\boldsymbol{x}, t) - \rho(\boldsymbol{x}, t) g +$$

$$\eta \left(\partial_j \partial_j u_i(\boldsymbol{x}, t) + \frac{\partial_i(\partial_j u_j(\boldsymbol{x}, t))}{3} \right). \tag{2}$$

Forming a coupled set of non-linear, partial differential equations for the velocity and pressure fields as functions of space $\boldsymbol{x}$ and time t, these represent mass and momentum conservation respectively, and must be satisfied by all Newtonian fluid phases within the system. For most practical applications, the fluids are assumed to be incompressible (have constant density) and so the continuity equation reduces to the incompressibility relation;

$$\partial_i u_i(\boldsymbol{x}, t) = 0. \tag{3}$$

This can be combined with equation 2 to give the incompressible Navier Stokes equation;

$$\rho \left(\frac{\partial u_i(\boldsymbol{x}, t)}{\partial t} + [u_j(\boldsymbol{x}, t) \partial_j] u_i(\boldsymbol{x}, t) \right) = -\partial_i P(\boldsymbol{x}, t) - \rho g + \eta \partial_j \partial_j u_i(\boldsymbol{x}, t). \tag{4}$$

The equations of motion can be expressed in an alternative form by defining the stress tensor $T_{ij}(\boldsymbol{x}, t)$ (Batchelor, 1967; Manga, 1994) and dynamic pressure $P_{\mathrm{d}}(\boldsymbol{x}, t)$:

$$T_{ij}(\boldsymbol{x}, t) = -P_{\mathrm{d}}(\boldsymbol{x}, t)\delta_{ij} + \eta[\partial_i u_j(\boldsymbol{x}, t) + \partial_j u_i(\boldsymbol{x}, t)], \tag{5}$$

$$P_{\mathrm{d}}(\boldsymbol{x}, t) = P(\boldsymbol{x}, t) - \rho g_i x_i, \tag{6}$$

where δ_{ij} are the components of the Kronecker delta tensor. This definition of the stress tensor removes the gravitational body force from the equations of motion, meaning that it only appears in the boundary conditions. The Navier Stokes equation then becomes

$$\rho\left(\frac{\partial u_i(\boldsymbol{x}, t)}{\partial t} + [u_j(\boldsymbol{x}, t)\partial_j]u_i(\boldsymbol{x}, t)\right) = \partial_j T_{ij}(\boldsymbol{x}, t). \tag{7}$$

When working in fluid dynamics, it is usual to non-dimensionalise the equations of motion and boundary conditions (White, 1999). This can be achieved by scaling the quantities involved by parameters specific to the problem. For example, consider a problem with typical scales of length L_{c} and velocity U_{c}. This allows us to define dimensionless variables (denoted by a $'$)

$$x_i = L_{\mathrm{c}} x_i', \tag{8}$$

$$u_i(\boldsymbol{x}, t) = U_{\mathrm{c}} u_i'(\boldsymbol{x}', t'), \tag{9}$$

and

$$t = \frac{L_{\mathrm{c}} t'}{U_{\mathrm{c}}}. \tag{10}$$

In the case of highly viscous flows the relevant scaling for the dynamic pressure uses a characteristic viscosity η_c and is given by (Lee and Leal, 1982)

$$P_d(\boldsymbol{x}, t) = \frac{\eta_c U_c P_d'(\boldsymbol{x'}, t')}{L_c}. \tag{11}$$

This choice of pressure scaling means that upon substitution of equations 8 to 11 into equation 5, the stress tensor can also be non-dimensionalised,

$$T_{ij}(\boldsymbol{x}, t) = \frac{\eta_c U_c T_{ij}'(\boldsymbol{x'}, t')}{L_c}, \quad \text{where} \quad T_{ij}'(\boldsymbol{x'}, t') = P_d'(\boldsymbol{x'}, t')\delta_{ij} + \Lambda[\partial_i' u_j'(\boldsymbol{x'}, t') + \partial_j' u_i'(\boldsymbol{x'}, t')], \tag{12}$$

where $\Lambda = \eta/\eta_c$. Hence, the dimensionless continuity and Navier Stokes equations are

$$\partial_i' u_i'(\boldsymbol{x'}, t') = 0, \tag{13}$$

and

$$Re\left(\frac{\partial u_i'(\boldsymbol{x'}, t')}{\partial t'} + (u_j'(\boldsymbol{x'}, t')\partial_j')u_i'(\boldsymbol{x'}, t')\right) = \partial_j' T_{ij}'(\boldsymbol{x'}, t'), \tag{14}$$

where the Reynolds number Re is defined as

$$Re = \frac{\rho L_c U_c}{\eta_c} \tag{15}$$

As we are considering the case of low Reynolds number (Re $\ll$ 1), we can neglect the inertial terms on the right hand side, and the equation reduces to the Stokes equation (Batchelor, 1967; Kim and Karrila, 2005)

$$\partial_i' T_{ij}'(\boldsymbol{x'}) = 0. \tag{16}$$

Note that the explicit time dependence has now vanished from the Stokes equations. However, it is still valid to use the equations for time dependent flows where the boundary conditions change with time, if the quasi-static assumption is satisfied;

$$\frac{L_c^2 \rho}{\eta_c} \ll \tau \tag{17}$$

where τ is a typical timescale for a change in flow geometry. Physically, this means that the velocity and stress fields of the fluid instantaneously respond to changes in the boundary conditions (Manga, 1994).

2.2 Boundary Conditions

In order to complete the formulation of any fluid dynamics problem, it is necessary to state the boundary conditions alongside the equations of motion (Riley et al., 2006). For fluids of infinite (or semi-infinite) extent in some dimension, these include the flow velocity at infinity. For bounded flows, the conditions are imposed at the boundaries of the fluid domain, and their exact nature depends on the phase of the material bounding it. At a boundary, two types of boundary condition can exist: a kinematic boundary condition on the velocity field and a dynamic boundary condition on the stress field (derivative of the velocity field). Kinematic boundary conditions are an expression of mass conservation and dynamic boundary conditions are a balance of forces, an expression of Newton's third law. Geometric symmetries can be exploited to identify further boundary conditions and reduce the complexity of problems. In unsteady flows, initial conditions are also important, but since we are considering quasi-static flows, we will not discuss these here.

2.2.1 Fluid-Solid Boundary

At low Reynolds number, for a fluid-solid boundary defined the surface $\mathcal{S}$ (see figure 1), the kinematic boundary condition usually employed is one of no-slip; the fluid velocity at the boundary is the same as that of the solid $U'_{s,i}$. This is easily expressed in dimensionless
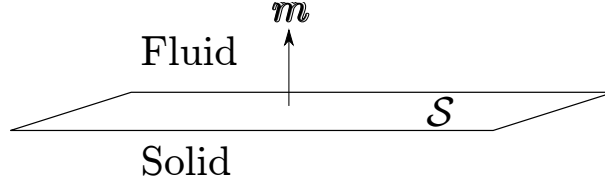
Figure 1: Fluid-solid boundary $\mathcal{S}$ with normal vector $\boldsymbol{m}$ directed into the fluid phase.

form as

$$u_i'(\boldsymbol{x}') = U_{\mathrm{s},i}', \quad \text{when } \boldsymbol{x} \in \mathcal{S}. \tag{18}$$

This is valid for situations when the fluid domain is much larger than the mean free path of molecules within the fluid. When this isn't true, a slip condition can be employed at the boundary (Dussan, 1976). There also needs to be a dynamic boundary condition applied at the interface. If the solid exerts a force F_i onto the fluid, then the condition states

$$\int_{\mathcal{S}} m_i(\boldsymbol{x}) T_{ij}(\boldsymbol{x}) \mathrm{d}\mathcal{S} = F_j, \tag{19}$$

where $m_i(\boldsymbol{x})$ is the normal vector to $\mathcal{S}$ directed into the fluid. Using the non-dimensionalisation scheme presented above this becomes

$$\eta_{\mathrm{c}} U_{\mathrm{c}} L_{\mathrm{c}} \int_{\mathcal{S}} f_i(\boldsymbol{x}') \mathrm{d}\mathcal{S}' = F_i, \tag{20}$$

where $f_i(\boldsymbol{x}') = m_i(\boldsymbol{x}') T_{ij}'(\boldsymbol{x}')$ is defined as the dimensionless traction vector on the surface $\mathcal{S}$, .

2.2.2   Fluid-Fluid Boundary

For a boundary $\mathcal{I}$ between two fluids labelled 1 and 2 (figure 2), the usual kinematic boundary condition states that the velocity of the two fluids must be continuous across
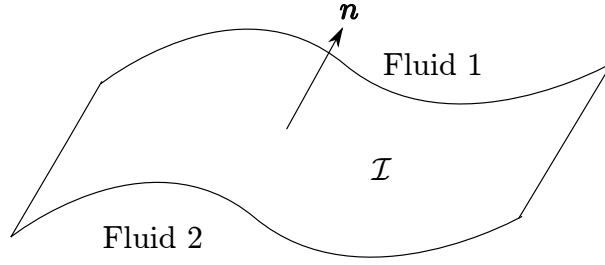
Figure 2: Fluid-fluid boundary $\mathcal{I}$ with normal vector $\boldsymbol{n}$.

the interface (Kim and Karrila, 2005). Defining the velocity of fluid l as u_l this can be expressed in dimensionless form as

$$u'_{1,i}(\boldsymbol{x'}) = u'_{2,i}(\boldsymbol{x'}), \quad \text{for } \boldsymbol{x'} \in \mathcal{I}. \tag{21}$$

Again, when fluid domains are small compared to the mean free path of molecules a slip condition can be employed (Maxwell, 1879). The dynamic boundary condition is an expression of the balance between the stress discontinuity across the interface and the interfacial tension (IFT) σ (Batchelor, 1967). With our definition of the stress tensor this is given as (Manga, 1994)

$$n_i(\boldsymbol{x})[T_{1,ij}(\boldsymbol{x}) - \rho_1 g_k x_k \delta_{ij}] - n_i(\boldsymbol{x})[T_{2,ij}(\boldsymbol{x}) - \rho_2 g_k x_k \delta_{ij}] = \tag{22}$$
$$\sigma(\boldsymbol{x}) n_j(\boldsymbol{x})[\partial_{\mathrm{s},i} n_i(\boldsymbol{x})] - \partial_{\mathrm{s},j} \sigma(\boldsymbol{x}), \quad \text{for } \boldsymbol{x} \in \mathcal{I},$$

where n_i is the normal vector to the surface $\mathcal{I}$ directed into fluid 1. The operator $\partial_{\mathrm{s},i}$ is defined as the tangential gradient operator within the surface $\mathcal{I}$:

$$\partial_{\mathrm{s},i} = (\delta_{ij} - \partial_i \partial_j) \partial_j. \tag{23}$$

When this takes the normal vector as its argument it can be shown that (Brackbill et al.,

1992)

$$\partial_{\mathrm{s},i} n_i = \partial_i n_i. \tag{24}$$

The presence of spatial gradients in the interfacial tension can lead to so-called Marangoni effects (Thomson, 1855; Gibbs, 1878). However, for our purposes we will assume that the interfacial tension is uniform across the interface $\mathcal{I}$, and so the last term on the right hand side vanishes;

$$n_i(\boldsymbol{x})[T_{1,ij}(\boldsymbol{x}) - \rho_1 g_k x_k \delta_{ij}] - n_i[T_{2,ij}(\boldsymbol{x}) - \rho_2 g_k x_k \delta_{ij}] = \tag{25}$$
$$\sigma(\boldsymbol{x}) n_i(\boldsymbol{x}) \partial_i n_j(\boldsymbol{x}), \quad \text{for } \boldsymbol{x} \in \mathcal{I}.$$

Like the equations of motion, this can be non-dimensionalised using equations 8 to 12

$$n_i(\boldsymbol{x}')[T'_{1,ij}(\boldsymbol{x}') - T'_{2,ij}(\boldsymbol{x}')]\,Ca + Bo(\hat{z}_i x'_i) n_j(\boldsymbol{x}') = n_j(\boldsymbol{x}')\partial'_i n_i(\boldsymbol{x}') \quad \text{for } \boldsymbol{x}' \in \mathcal{I}. \tag{26}$$

The capillary number Ca and Bond number Bo are dimensionless numbers defined as:

$$Ca = \frac{\eta_{\mathrm{c}} U_{\mathrm{c}}}{\sigma}, \tag{27}$$

and

$$Bo = \frac{(\rho_2 - \rho_1) g L_{\mathrm{c}}^2}{\sigma}. \tag{28}$$

2.3 Greens functions

In order to derive the integral representation of the Stokes equations, it is necessary to make use of the Greens functions (Riley et al., 2006) for Stokes flow, $\hat{u}_i(\boldsymbol{x}' - \boldsymbol{y}')$ and

$\hat{T}_{ij}(\boldsymbol{x'} - \boldsymbol{y'})$, defined such that (Kim and Karrila, 2005)

$$\partial_i' \hat{u}_i(\boldsymbol{x'} - \boldsymbol{y'}) = 0, \tag{29}$$

and

$$\partial_i' \hat{T}_{ij}(\boldsymbol{x'} - \boldsymbol{y'}) + \mathcal{F}_j \delta(\boldsymbol{x'} - \boldsymbol{y'}) = 0, \tag{30}$$

where $\mathcal{F}_i$ is a arbitrary constant vector, $\delta(\boldsymbol{x'} - \boldsymbol{y'})$ is the Dirac delta-function (appendix A) and both $\hat{u}_i(\boldsymbol{x'})$ and $\hat{T}_{ij}(\boldsymbol{x'}) \to 0$ as $|\boldsymbol{x'}| \to \infty$. Equations 29 and 30 can be solved following Ladyzhenskaya (1963) to show that (see appendix B) (Kim and Karrila, 2005)

$$\hat{u}_j(\boldsymbol{\xi}) = \frac{\mathcal{F}_i J_{ij}(\boldsymbol{\xi})}{\Lambda}, \tag{31}$$

and

$$\hat{T}_{ij}(\boldsymbol{\xi}) = K_{ijk}(\boldsymbol{\xi})\mathcal{F}_k, \tag{32}$$

where $\boldsymbol{\xi} = \boldsymbol{x'} - \boldsymbol{y'}$,

$$J_{ij}(\boldsymbol{\xi}) = \frac{1}{8\pi\xi}\left(\delta_{ij} + \frac{\xi_i\xi_j}{\xi^2}\right), \tag{33}$$

and

$$K_{ijk}(\boldsymbol{\xi}) = \frac{-3\xi_i\xi_j\xi_k}{4\pi\xi^5}. \tag{34}$$

We have defined $\xi = \xi_i\xi_i$.

2.4 Integral Representation of Stokes Equations

We now substitute the Greens functions and unknown velocity and stress field solutions into the Lorentz Reciprocal Theorem (equation 124 in appendix C) and simplfify using equations 16 and 30 to find

$$\oint_{\mathcal{V}} u'_k(\boldsymbol{x'})\delta(\boldsymbol{\xi})\mathrm{d}\boldsymbol{x'}^3 = \frac{1}{\Lambda}\oint_{\mathcal{S}} J_{ik}(\boldsymbol{\xi})T'_{ij}(\boldsymbol{x'})n_j(\boldsymbol{x'})\mathrm{d}\boldsymbol{x'}^2 - \oint_{\mathcal{S}} u'_i(\boldsymbol{x'})K_{ijk}(\boldsymbol{\xi})n_j(\boldsymbol{x'})\mathrm{d}\boldsymbol{x'}^2. \quad (35)$$

Here the integrals are defined in the sense of the Cauchy Principle Value (CPV) to account for the possibility that the kernels J_{ij} and K_{ijk} have singular points in the range of integration. Finally make the transformation $\boldsymbol{x'} \leftrightarrow \boldsymbol{y'}$ and use the symmetry properties of the kernels (equations 110 and 111 in appendix B) and the delta function (equation 87 in appendix A) to obtain the general form of the integral representation of the Stokes equations;

$$\oint_{\mathcal{V}} u'_k(\boldsymbol{y'})\delta(\boldsymbol{\xi})\mathrm{d}\boldsymbol{y'}^3 = \frac{1}{\Lambda}\oint_{\mathcal{S}} J_{ik}(\boldsymbol{\xi})T'_{ij}(\boldsymbol{y'})n_j(\boldsymbol{y'})\mathrm{d}\boldsymbol{y'}^2 + \oint_{\mathcal{S}} u'_i(\boldsymbol{y'})K_{ijk}(\boldsymbol{\xi})n_j(\boldsymbol{y'})\mathrm{d}\boldsymbol{y'}^2. \quad (36)$$

Using the definition of the delta function (equation 85 in appendix A) this means

$$\frac{1}{\Lambda}\oint_{\mathcal{S}} J_{ik}(\boldsymbol{\xi})T'_{ij}(\boldsymbol{y'})n_j(\boldsymbol{y'})\mathrm{d}\boldsymbol{y'}^2 + \oint_{\mathcal{S}} u'_i(\boldsymbol{y'})K_{ijk}(\boldsymbol{\xi})n_j(\boldsymbol{y'})\mathrm{d}\boldsymbol{y'}^2 = \begin{cases} u'_k(\boldsymbol{x'}) & \boldsymbol{x'} \in \mathcal{V} \\ \frac{u'_k(\boldsymbol{x'})}{2} & \boldsymbol{x'} \in \mathcal{S} \\ 0 & \text{otherwise} \end{cases} . \quad (37)$$

3   Theoretical Development

3.1   Problem Statement

We are interested in the low Reynolds number, on-axis gravitational settling of a spheroid towards a fluid-fluid interface (figure 3). We denote the upper(lower) phase as fluid 1(2). The physical parameters motivate the choice of scaling variables. The characteristic lengthscale is chosen to be the horizontal minor axis a, characteristic viscosity that of the upper fluid η_1, and characteristic velocity to be the terminal velocity of a sphere of radius a in the upper fluid(Reynolds, 1886)

$$U_{\mathrm{c}} = \frac{2(\rho_{\mathrm{s}} - \rho_1)ga^2}{9\eta_1},\tag{38}$$

where ρ_1 is the density of fluid 1, ρ_{s} the spheroid density, and $g = 9.81$ m s^{-1} the acceleration due to gravity. Defining ρ_2 as the density of fluid 2 and σ as the IFT, this means the capillary and Bond numbers can be expressed as

$$Ca = \frac{(\rho_{\mathrm{s}} - \rho_1)ga^2}{\sigma},\tag{39}$$

and

$$Bo = \frac{(\rho_2 - \rho_1)ga^2}{\sigma}.\tag{40}$$

The dimensionless stress tensor for each fluid can be written as

$$T'_{\alpha,ij}(\boldsymbol{x'}) = -P'_{\mathrm{d},l}(\boldsymbol{x'})\delta_{ij} + \Lambda_l[\partial'_i u'_{l,j}(\boldsymbol{x'}) - \partial'_j u'_{l,i}(\boldsymbol{x'})],\tag{41}$$

where $P'_{\mathrm{d},l}$ and $u'_{l,i}$ are the dimensionless dynamic pressure and velcoity fields in fluid l respectively. We use l to denote the fluid and i,j to denote tensoral components. The
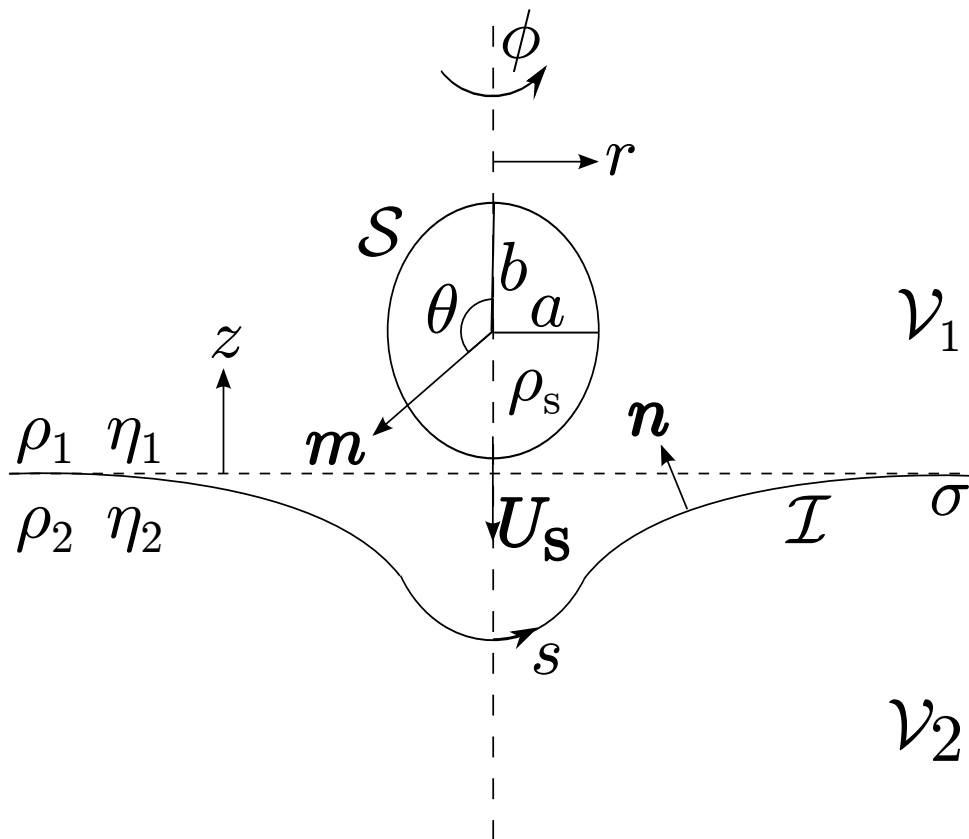
Figure 3: Diagrammatic representation of the system. A spheroid falls on-axis under gravity, at low Reynolds number, towards an initially horizontal interface between two density stratified, immiscible, semi-infinite fluids.

parameter Λ_l is defined as

$$\Lambda_l = \frac{\eta_l}{\eta_1} = \begin{cases} 1, & l = 1 \\ \frac{\eta_2}{\eta_1} = \lambda, & l = 2 \end{cases}.$$ (42)

where η_2 is the dynamic viscosity of the lower phase. Note λ is the viscosity ratio of the two fluids. Additionally $\mathcal{V}_{1(2)}$ dentotes the volume of fluid 1(2), $\mathcal{I}$ the interface and $\mathcal{S}$ the spheroid surface. $\boldsymbol{m}$ and $\boldsymbol{n}$ are the normal vectors to the spheroid surface and interface respectively and both are directed into fluid 1. We use cylindrical polar coordinates to describe the system with r the radial coordinate with respect to the symmetry axis, ϕ the azimuthal coordinate, and z the vertical coordinate with respect to the plane of the initial, undeformed interface. Additionally we make use of the polar angle θ defined with respect to the centre of the spheroid, and the arc-length s defined as the distance along the interface from the symmetry axis in any azimuthal plane.

It is straightforward to apply the general equations of motion and boundary conditions to the problem. The equations of motion, which must be satsified in both fluid domains, appear as

$$\partial_i' u_{l,i}'(\boldsymbol{x}') = 0,$$ (43)

and

$$\partial_i' T_{l,ij}'(\boldsymbol{x}') = 0.$$ (44)

The first boundary condition that we impose is that the undisturbed fluid is quiescent, so the velocity field is constrained to decay away from the sphere;

$$u_{l,i}'(\boldsymbol{x}') \to 0 \text{ as } |\boldsymbol{x}'| \to \infty.$$ (45)

13

The kinematic boundary condition on the fluid interface (equation 21) can be expressed as

$$u'_{1,i}(\boldsymbol{x}') = u'_{2,i}(\boldsymbol{x}'), \quad \boldsymbol{x}' \in \mathcal{I}. \tag{46}$$

The dynamic boundary condition is also imposed at the interface;

$$n_i(\boldsymbol{x}')[T'_{1,ij}(\boldsymbol{x}') - T'_{2,ij}(\boldsymbol{x}')]Ca + \hat{z}_i x'_i n_j(\boldsymbol{x}')Bo = n_j(\boldsymbol{x}')\partial'_i n_i(\boldsymbol{x}'), \quad \text{for } \boldsymbol{x}' \in \mathcal{I}. \tag{47}$$

However we can define the modified density ratio (MDR) D as

$$D = \frac{Ca}{Bo} = \frac{\rho_s - \rho_1}{\rho_2 - \rho_1}. \tag{48}$$

This means equation 47 can be re-expressed as

$$n_i(\boldsymbol{x}')[T'_{1,ij}(\boldsymbol{x}') - T'_{2,ij}(\boldsymbol{x}')]DBo = n_j(\boldsymbol{x}')[\partial'_i n_i(\boldsymbol{x}') - \hat{z}_i x'_i Bo], \quad \text{for } \boldsymbol{x}' \in \mathcal{I}. \tag{49}$$

The kinematic boundary condition on the spheroid surface is

$$u'_{1,i}(\boldsymbol{x}') = U'_{s,i}, \quad \boldsymbol{x}' \in \mathcal{S}. \tag{50}$$

where $U_{s,i}$ is the velocity of the spheroid. The final boundary condition is the dynamic boundary condition on the spheroid. The force on the fluid due to the spheroid originates from the balance between gravity and buoyancy;

$$F_i = -\frac{4\pi a^2 b(\rho_s - \rho_1)g\hat{z}_i}{3}, \tag{51}$$

where b is the vertical minor axis. Substituting this into equation 20 and using equation 38 we obtain

$$\int_{\mathcal{S}} f_i(\boldsymbol{x}')\mathrm{d}\mathcal{S}' = -6\pi\hat{z}_i. \tag{52}$$

Defining the aspect ratio of the spheroid $R = b/a$, the dimensionless numbers that describe the system are the set $\{\lambda, D, Bo, R\}$.

3.2 Integral Representation

To recast the problem in an integral representation, we need to apply equation 37 to each fluid separately. The domain of fluid 1 is bound by the spheroid surface and interface, and extends to infinity as $r, z \to \infty$. The boundary condition at infinity (equation 45) ensures that the far-field contribution to the surface integrals in equation 37 vanishes, meaning that just the spheroid surface and interface contribute. Additionally the no-slip boundary condition on the spheroid surface (equation 50), the divergence theorem (appendix E) and the definition of the Greens function for pressure (equation 30) can be used to show that the integral of $u'_{1,i}(\boldsymbol{y}')K_{ijk}(\boldsymbol{\xi})m_j(\boldsymbol{y}')$ over the spheroid surface vanishes. Hence the boundary integral equation for fluid 1 can be written as

$$\oint_{\mathcal{S}} J_{ik}(\boldsymbol{\xi})T'_{1,ij}(\boldsymbol{y}')m_j(\boldsymbol{y}')\mathrm{d}^2\boldsymbol{y}' + \oint_{\mathcal{I}} J_{ik}(\boldsymbol{\xi})T'_{1,ij}(\boldsymbol{y}')n_j(\boldsymbol{y}')\mathrm{d}^2\boldsymbol{y}' +$$
$$\oint_{\mathcal{I}} u'_{1,i}(\boldsymbol{y}')K_{ijk}(\boldsymbol{\xi})n_j(\boldsymbol{y})\mathrm{d}^2\boldsymbol{y}' = \begin{cases} \frac{u'_{1,k}(\boldsymbol{x}')}{2} & \boldsymbol{x}' \in \mathcal{I} \\ u'_{s,k} & \boldsymbol{x}' \in \mathcal{S} \end{cases}. \tag{53}$$

For fluid 2, the contribution to the surface integrals at infinity again vanishes leaving just a contribution from the interface. Using the kinemtic boundary condition at the interface

(equation 46) the boundary integral equation for fluid 2 can be written as

$$-\oint_{\mathcal{I}} J_{ik}(\boldsymbol{\xi})T'_{1,ij}(\boldsymbol{y'})n_j(\boldsymbol{y'})\mathrm{d}^2\boldsymbol{y'} - \lambda\oint_{\mathcal{I}} u'_{1,i}(\boldsymbol{y'})K_{ijk}(\boldsymbol{\xi})n_j(\boldsymbol{y})\mathrm{d}^2\boldsymbol{y'} = \frac{\lambda u'_{1,k}(\boldsymbol{x'})}{2} \quad \boldsymbol{x'} \in \mathcal{I}, \quad (54)$$

where the minus sign occurs since the normal vector is directed out of fluid 2. Equations 53 and 54 can be added together and combined with equation 49 to obtain

$$\oint_{\mathcal{S}} J_{ik}(\boldsymbol{\xi})f_{\mathrm{s},i}(\boldsymbol{y'})\mathrm{d}^2\boldsymbol{y'} + \frac{9}{2\mathrm{DBo}}\oint_{\mathcal{I}} J_{ik}(\boldsymbol{\xi})n_i(\boldsymbol{y'})[\partial'_j n_j(\boldsymbol{y'}) - \hat{z}_j y'_j\mathrm{Bo}]\mathrm{d}^2\boldsymbol{y'}+$$
$$(1-\lambda)\oint_{\mathcal{I}} u'_{1,i}(\boldsymbol{y'})K_{ijk}(\boldsymbol{\xi})n_j(\boldsymbol{y'})\mathrm{d}^2\boldsymbol{y'} = \begin{cases} \frac{(1+\lambda)u'_{1,k}(\boldsymbol{x'})}{2} & \boldsymbol{x'} \in \mathcal{I} \\ u'_{s,k} & \boldsymbol{x'} \in \mathcal{S} \end{cases}. \quad (55)$$

This together with equation 52 completely describes the system in an integral representation.

3.3   Axisymmetric Simplification

We can exploit the axial symmetry of the system to chose the point $\boldsymbol{x'}$ such that it lies in the plane defined by $\phi = 0$. Hence in Cartesian coordinates $\boldsymbol{x'} = (x_r, 0, x_z)$. This also means we can write $\boldsymbol{y'} = (y_r \cos\phi, y_r \sin\phi, y_z)$. On the surface of the spheroid $y_r = y_r(\theta)$ and $y_z = y_z(\theta)$, and on the interface $y_r = y_r(s)$ and $y_z = y_z(s)$. Additionally $\boldsymbol{f} = [f_r(\theta)\cos\phi, f_r(\theta)\sin\phi, f_z(\theta)]$ and $\boldsymbol{n} = [n_r(s)\cos\phi, n_r(s)\sin\phi, n_z(s)]$. Since the system is axisymmetric, it is useful to extract the azimuthal integration from the surface integrals in equations 52 and 55. To achieve this, the Cartesian components of each equation are considered separately. For equation 55, it can be shown that both the left and right hand sides of the 2-component equation are identically zero. For equation 52 this is true for the 1- and 2-components. To show this, J_{ij} and K_{ijk} are first expanded in terms of in terms of the components of $\boldsymbol{x'}$ and $\boldsymbol{y'}$ before the integration over ϕ is carried out. This leaves three integral equations which can be expressed as

$$R \int_{\theta=0}^{\pi} B_{\alpha\beta}(\boldsymbol{x}',\theta)\Phi_{\beta}(\theta)\mathrm{d}\theta + \int_{s=0}^{\infty} \left(A_{\alpha\beta}(\boldsymbol{x}',s)y_r(s) - \frac{(1+\lambda)\delta_{\alpha\beta}\delta(s-s_0)}{2} \right) \Psi_{\beta}(s)\mathrm{d}s$$

$$= -\int_{s=0}^{\infty} C_{\alpha}(\boldsymbol{x}',s)y_r(s)\mathrm{d}s, \quad \text{for } \boldsymbol{x}' \in \mathcal{I}, \quad (56)$$

$$R \int_{\theta=0}^{\pi} B_{\alpha\beta}(\boldsymbol{x}',\theta)\Phi_{\beta}(\theta)\mathrm{d}\theta + \int_{s=0}^{\infty} A_{\alpha\beta}(\boldsymbol{x}',s)\Psi_{\beta}(s)y_r(s)\mathrm{d}s - \Theta_{\alpha} = \int_{s=0}^{\infty} C_{\alpha}(\boldsymbol{x}',s)y_r(s)\mathrm{d}s, \quad \text{for } \boldsymbol{x}' \in \mathcal{S},$$

$$(57)$$

and

$$\int_{\theta=0}^{\pi} \Phi_2(\theta)\mathrm{d}\theta = -3, \quad (58)$$

where the quantities $\boldsymbol{A}$, $\boldsymbol{B}$, $\boldsymbol{C}$, $\boldsymbol{\Psi}$, $\boldsymbol{\Phi}$ and $\boldsymbol{\Theta}$ are defined as:

$$\boldsymbol{A} = (1-\lambda) \int_{\phi=0}^{2\pi} \begin{pmatrix} n_r(K_{111}\cos^2\phi + K_{221}\sin^2\phi + 2K_{121}\sin\phi\cos\phi) & n_r(K_{131}\cos\phi + K_{231}\sin\phi) \\ \quad + n_z(K_{131}\cos\phi + K_{231}\sin\phi) & \quad + n_z K_{331} \\ n_r(K_{113}\cos^2\phi + K_{223}\sin^2\phi + 2K_{123}\sin\phi\cos\phi) & n_r(K_{133}\cos\phi + K_{233}\sin\phi) \\ \quad + n_z(K_{133}\cos\phi + K_{233}\sin\phi) & \quad + n_z K_{333} \end{pmatrix} \mathrm{d}\phi,$$

$$(59)$$

$$\boldsymbol{B} = \int_{\phi=0}^{2\pi} \begin{pmatrix} J_{11}\cos\phi + J_{21}\sin\phi & J_{31} \\ J_{13}\cos\phi + J_{23}\sin\phi & J_{33} \end{pmatrix} \mathrm{d}\phi, \quad (60)$$

$$\boldsymbol{C} = \frac{9(\partial_j' n_j - \mathrm{Bo}y_z)}{2D\mathrm{Bo}} \int_{\phi=0}^{2\pi} \begin{pmatrix} n_r(J_{11}\cos\phi + J_{21}\sin\phi) + n_z J_{31} \\ n_r(J_{13}\cos\phi + J_{23}\sin\phi) + n_z J_{23} \end{pmatrix} \mathrm{d}\phi, \quad (61)$$

$$\boldsymbol{\Psi} = \begin{pmatrix} u_{1,r}'(s) \\ u_{1,z}'(s) \end{pmatrix}, \quad (62)$$

$$\boldsymbol{\Phi} = \begin{pmatrix} f_{s,r}(\theta) \\ f_{s,z}(\theta) \end{pmatrix} \sin^2\theta \left(1 + \frac{\cot^2\theta}{R^2}\right)^{1/2}, \tag{63}$$

and

$$\boldsymbol{\Theta} = \begin{pmatrix} 0 \\ u'_s \end{pmatrix} \tag{64}$$

For brevity, the function arguments have been dropped from the kernels and the normal vectors but $n_i = n_i[\boldsymbol{y}'(s,\phi)]$ and in equation 59, $K_{ijk} = K_{ijk}[\boldsymbol{x}' - \boldsymbol{y}'(s,\phi)]$, in equation 60, $J_{ij} = J_{ij}[\boldsymbol{x}' - \boldsymbol{y}'(\theta,\phi)]$ and in equation 61, $J_{ij} = J_{ij}[\boldsymbol{x}' - \boldsymbol{y}'(s,\phi)]$.

The aziumthal integrals inside the definitions of $\boldsymbol{A}$, $\boldsymbol{B}$ and $\boldsymbol{C}$ can be expressed as sums of complete elliptic integrals of the first and second kind (Lee and Leal, 1982; Geller et al., 1985; Graziani, 1989; Pozrikids, 1992; Manga, 1994; Roumeliotis, 2000) which can then be evaluated using polynomial expansions (Abramowitz and Stegun, 1972). Details of this are given in appendices F and G.

4 Numerical Method

Equations 56 to 58 are a coupled set of integral equations for the unknowns $\boldsymbol{\Psi}(s)$, $\boldsymbol{\Phi}(\theta)$ and $\boldsymbol{\Theta}$. These solutions can be found numerically by discretising the system, allowing the integral equations to be expressed as a linear system of algerbraic equations which are then solved using LU decomposition and Gaussian elimination (Riley et al., 2006; Press et al., 2007). Once the interfacial and sphere velocities are solved for, the system is iterated forward in time, and the process is repeated.
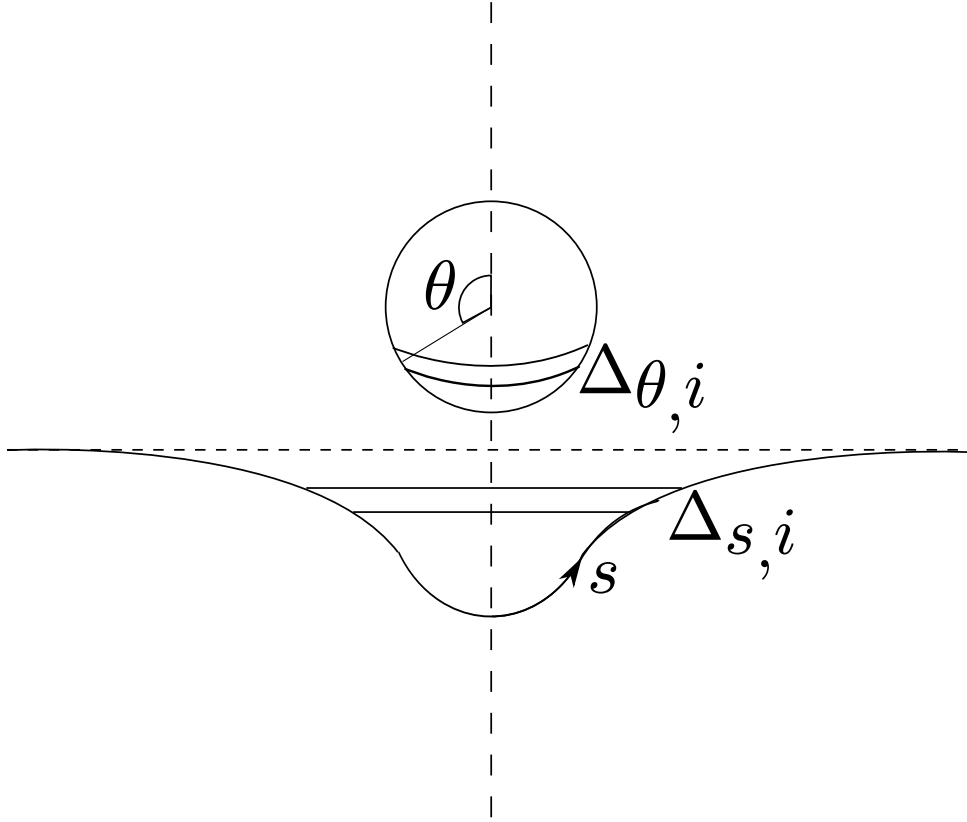
Figure 4: Diagrammatic representation of the discretisation of the system. Both interface and spheroid surface are divided into axisymmetric rings centred on the symmetry axis.

4.1   Discretisation and Linear System

To discretise the set of equations, the interface and sphere surface are divided into intervals. The interface is divided into N axisymmetric rings, where the ith ring is centred at arc-length s_i and is of thinkness $\Delta_{s,i}$. The interface is truncated at the arc-length s_N. The sphere surface is discretised in M axisymmetric rings, where the ith ring is centred at polar coordinate θ_i and has a thickness $\Delta_{\theta,i}$. A schematic of the discretisation scheme is depicted in figure 4.

We now choose $\boldsymbol{x}' = \boldsymbol{x}_i$ where $\boldsymbol{x}_i = \boldsymbol{x}_i(\theta_i)$ on $\mathcal{S}$ and $\boldsymbol{x}_i = \boldsymbol{x}_i(s_i)$ on $\mathcal{I}$. That is, the point $\boldsymbol{x}'$ is chosen to be the midpoint of one of the intervals. Then, we can express the integrals as discrete sums over each element. We then make the approximation that the unknowns $\boldsymbol{\Psi}(s)$ and $\boldsymbol{\Phi}(\theta)$ are constant over the width of an interval and for interval i, $\boldsymbol{\Psi}(s) = \boldsymbol{\Psi}(s_i)$

and $\boldsymbol{\Phi}(\theta) = \boldsymbol{\Phi}(\theta_i)$. This allows us to obtain the discrete form of the integral equations:

$$R\sum_{i=1}^{M}\Phi_\beta(\theta_i)\int_{\Delta_{\theta,i}}B_{\alpha\beta}(s_j,\theta)\mathrm{d}\theta + \sum_{i=1}^{N}\Psi_\beta(s_i)\int_{\Delta_{s,i}}\left(A_{\alpha\beta}(s_j,s)y_r(s) - \frac{(1+\lambda)\delta_{\alpha\beta}\delta(s-s_j)}{2}\right)\mathrm{d}s$$
$$= -\sum_{i=1}^{N}\int_{\Delta_{s,i}}C_\alpha(s_j,s)y_r(s)\mathrm{d}s,$$

$$(65)$$

$$R\sum_{i=1}^{M}\Phi_\beta(\theta_i)\int_{\Delta_{\theta,i}}B_{\alpha\beta}(\theta_j,\theta)\mathrm{d}\theta + \sum_{i=1}^{N}\Psi_\beta(s_i)\int_{\Delta_{s,i}}A_{\alpha\beta}(\theta_j,s)y_r(s)\mathrm{d}s - \Theta_\alpha = -\sum_{i=1}^{N}\int_{\Delta_{s,i}}C_\alpha(\theta_j,s)y_r(s)\mathrm{d}s,$$

$$(66)$$

and

$$\sum_{i=1}^{M}\Phi_2(\theta_i)\int_{\Delta_{\theta,i}}\mathrm{d}\theta = -3. \tag{67}$$

This is seemingly a set of $2(N + M) + 1$ linear equations for $2(N + M) + 1$ unknowns; $\Phi_\alpha(\theta_i)$, $\Psi_\alpha(s_j)$ and Θ_1 (recall that $\Theta_2 = 0$) where $\alpha = 1, 2$, $i = 1, 2, ..., M$ and $j = 1, 2, ..., N$. However we can use physical arguments to simplify the system further. First by symmetry, the radial interfacial velocity must vanish on the symmetry axis i.e. $\Psi_1(s_1) = 0$. Additionally, the on-axis radial tractions on the sphere must also vanish meaning $\Phi_1(\theta_1) = \Phi_1(\theta_M) = 0$. Indeed, it can be shown that the coefficients of these terms vanish by using the expressions for $A_{\alpha\beta}$, $B_{\alpha\beta}$ and C_α, given in appendix G.1. Hence the equations where these terms appear are redundant and can be removed from the linear system. This leaves us with a system of $2(N + M - 1)$ linear equations for $2(N + M - 1)$ unknowns.

4.2 Evaluation of the coefficients

These equations can be recast as a matrix equation $L_{\mu\nu}X_\mu = Y_\nu$ where the unknown quantities are the elements X_μ. The elements $L_{\mu\nu}$ and Y_ν are the coefficients of the

Table 1: The order of the singularity of the components of $\boldsymbol{A}$, $\boldsymbol{B}$ and $\boldsymbol{C}$.

A_{11}	$1/\epsilon$	B_{11}	$\ln|\epsilon|$	C_1	$\ln|\epsilon|$
A_{12}	0	B_{12}	0	C_2	$\ln|\epsilon|$
A_{21}	0	B_{21}	0		
A_{22}	0	B_{22}	$\ln|\epsilon|$		

system and contain integrals that need to be evaluated numerically. If $\boldsymbol{x'}_j$ is not within the range of integration, then this is done using 4-point Gaussian-Legendre quadrature (Riley et al., 2006). However if $\boldsymbol{x'}_j$ is in the integration range, then the integrand is singular at the point $\boldsymbol{y'} = \boldsymbol{x'}_j$ and care needs to be taken when evaluating the integral. First, the order of the singularity needs to be determined. To do this, write $\boldsymbol{y'} = \boldsymbol{x'}_j + \epsilon\boldsymbol{t}$, where $\epsilon = \theta - \theta_j$ on the sphere, and $\epsilon = s - s_j$ on the interface, and $\boldsymbol{t}$ is the tangent to the curve. The integrands are then expanded in terms of ϵ. The order of the singularity if the order of the first order singular term in ϵ. Table 1 shows the order of the singularity of each component of $\boldsymbol{A}$, $\boldsymbol{B}$ and $\boldsymbol{C}$.

We then re-write the integrand as the sum of a regular and singular part. Denoting the integrand by $I(\zeta, \zeta_i)$ (where ζ represents θ or s depending on whether the integration is over the sphere or the interface) this can be written as $I(\zeta, \zeta_i) = I_r(\zeta, \zeta_i) + I_s(\zeta, \zeta_i)$ where I_r is the regular part and I_s is the singular part. The singular part can then be written as

$$I(\zeta, \zeta_i)_s = [I_s(\zeta, \zeta_i) - L(\zeta, \zeta_i)] + L(\zeta, \zeta_i), \tag{68}$$

where L is the leading order contribution to I_s. The terms in square parenthesese now form a regular function which can be integrated numerically. For the case that the integral is $1/\epsilon$ singular, the final term can be expressed as

$$L(\zeta, \zeta_i) = \frac{g(\zeta, \zeta_i)}{\epsilon} = \frac{g(\zeta, \zeta_i) - g(\zeta_i, \zeta_i)}{\epsilon} + \frac{g(\zeta_i, \zeta_i)}{\epsilon}. \tag{69}$$

Similarly, if the integral if $\ln|\epsilon|$ singular

$$L(\zeta, \zeta_i) = g(\zeta, \zeta_i) \ln|\epsilon| = [g(\zeta, \zeta_i) - g(\zeta_i, \zeta_i)] \ln|\epsilon| + g(\zeta_i, \zeta_i) \ln|\epsilon| \tag{70}$$

In both these cases, the first term on the right hand side is regular and the last term is singular but can be integrated analytically. This means that the irregular integrand can be expressed as the sum of a regular function, that can be integrated numerically, and an irregular function, that can be integrated analytically.

To calculate integrals over the interface, it is necessary to evaluate the components of the normal vector and its divergence at discrete points along the interface. To do this, cubic splines are fitted to the collocation points describing the interface (WAITING FOR DE BOER BOOK TO REF THIS) using routines given in Press et al. (2007) so that the interface is described parametrically with $r = r(s)$ and $z = z(s)$. Remembering that for a surface $H(r, z) = z - f(r)$, the components of the normal vector are given by $n_i = \partial_i H / (\partial_j H \partial_j H)$ (Riley et al., 2006), the following expressions can be obtained

$$n_r(s) = \frac{-\dot{z}}{(\dot{r} + \dot{z})^{1/2}}, \tag{71}$$

$$n_z(s) = \frac{\dot{r}}{(\dot{r} + \dot{z})^{1/2}}, \tag{72}$$

and

$$\partial_i' n_i = \frac{\dot{z}}{r(\dot{r} + \dot{z})^{1/2}} + \frac{\dot{r}\ddot{z} - \ddot{r}\dot{z}}{(\dot{r} + \dot{z})^{3/2}}. \tag{73}$$

These expressions are given in given in (Manga, 1994) except for a minus sign error in the components of the normal. The derivatives of the splines are calculated numerically using routines modified from Press et al. (2007). Once all of the elements $L_{\mu\nu}$ and Y_ν have been calculated the system of equations is solved by Lower-Upper (LU) decomposition

and Gaussian elimination (Riley et al., 2006; Press et al., 2007) using routines from the GNU Scientific Library (GSL) (Galassi et al., 2009).

4.3 Temporal Iteration

The system is iterated forward in time using an explicit first order Euler method (Manga, 1994) with timestep Δt. This means the position of the sphere z_s at time $t + \Delta t$ is found using

$$z_s(t' + \Delta t') = U'_s(t)\Delta t', \tag{74}$$

and the position of the collocation points on the interface moves according to

$$x_r(s_i, t' + \Delta t') = u_r(s_i, t')\Delta t', \tag{75}$$

and

$$x_z(s_i, t' + \Delta t') = u_z(s_i, t')\Delta t'. \tag{76}$$

There are both numerical and physical constraints on the value of the timestep. Numerically, it is limited by the Courant-Friedrich-Lewy (CFL) criterion Courant28. Physically, it is neccessary to ensure that it is smaller than the timescale over which different processes can occur. Owing to the multi-component nature of this problem, there are four timescales instrinsic to the problem: the Stokes timescale in the upper fluid $\tau_{s,1} = 9\eta_1/[2(\rho_s - \rho_1)ga]$, the Stokes timescale in the lower fluid $\tau_{s,2} = 9\eta_2/[2(\rho_s - \rho_2)ga]$, the capilary time for the upper fluid $\tau_{c,1} = \eta_1 a/\sigma$ and the capilary time for the lower fluid $\tau_{c,2} = \eta_2 a/\sigma$. It is required that the timestep is smaller than all of these so that the physics occuring on each timescale can be resolved. Non-dimensionalising each of these timescales we find that in dimensionless form they exist as $\tau'_{s,1} = 1$, $\tau'_{s,2} = \lambda D/(D-1)$, $\tau'_{c,1} = 2DBo/9$,

$\tau'_{c,2} = 2DBo\lambda/9$. Hence, for each simulation, the shortest physical timescale is identified and the timestep is constrained to be smaller than this throughout the simulation. The timestep is allowed to change during the simulation such that it is as large as can be allowed by both the CFL and numerical criteria.

Due to gradients in the velocity tangential to the fluid interface, the distribution of collocation points is altered during this time stepping process, so the collocation points are redistributed between each time step. Following the redistribution, the linear system is reconstructed for the new geometry and solved using the same procedure. The process continues in this fashion until the separtation between the sphere and the interface, or two different parts of the interface equals the local separation between collocation points, as the discretisation no longer provides an accurate approximation to the continuous system

5   Model Testing

5.1   Uniform and Infinite Fluid

To test the model, we can remove the interface and fluid 2, leaving us with the problem of the steady gravitational settling of a spheroid through fluid 1, which is uniform and infinite in extent. The terminal velocity of a spheroid settling on axis can be solved for analytically (Happel and Brenner, 1973) and in our dimensionless scheme is given by

$$U'_t = \frac{1}{K},\tag{77}$$

where

$$K = \begin{cases} \frac{4}{3(\mu^2+1)^{1/2}[\mu-(\mu^2-1)\cot^{-1}\mu]} & \text{for } R < 1 \\[2ex] \frac{4}{3(\mu^2-1)^{1/2}[(\mu^2+1)\coth^{-1}\mu-\mu]} & \text{for } R > 1 \\[2ex] 1 & \text{for } R = 1, \end{cases}\tag{78}$$
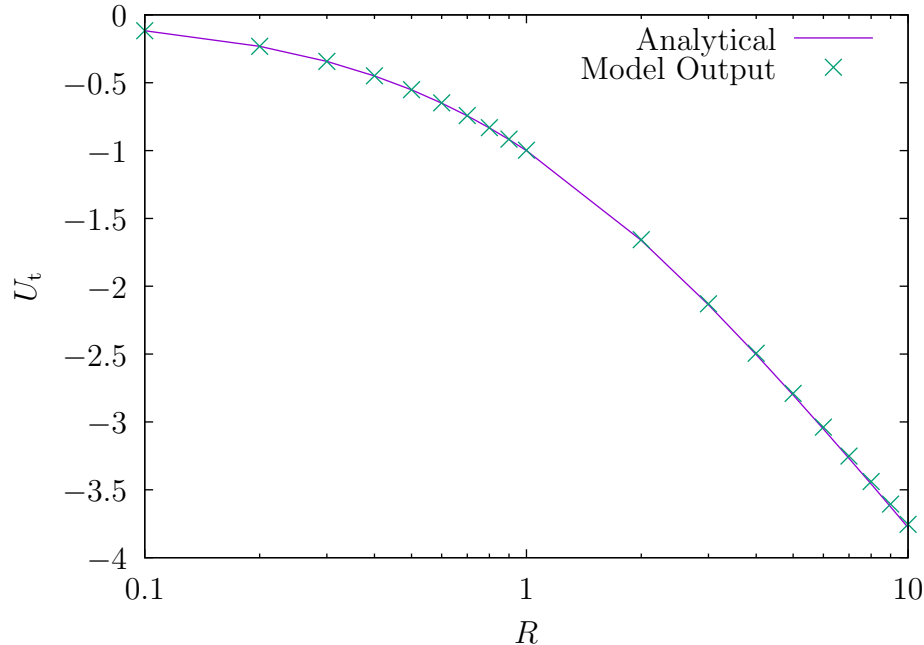
Figure 5: Curve shows analytical solution for dimensionless terminal velocity vs. aspect ratio (equation 78). Points show calculated values from model. There is excellent agreement for oblate spheroids but the error increases with aspect ratio.

and

$$\mu = \frac{R}{|R^2 - 1|^{1/2}}. \tag{79}$$

For the case that $\lambda = 1$, and a flat interface, the integrals over the interface in equations 65 to 67 vanish and the system reduces to that of the case of a spheroid settling in an infinite and uniform fluid. Figure 5 shows the analytical result for the terminal velocity from Happel and Brenner (1973) compared with that calculated by our model. It can be seen that agreement is excellent for aspect ratios in the range 0.1-10.

We tested the senstivity of the results to the number of intervals on the sphere. Figure 6 shows the fractional error on the calculated terminal velocity as a function of the number of intervals used to discretise the sphere M, for both a prolate and oblate spheroid, and a sphere. For $M \geq 100$, the fractional error is less than 0.003. It is also clear here that the error increases with R.
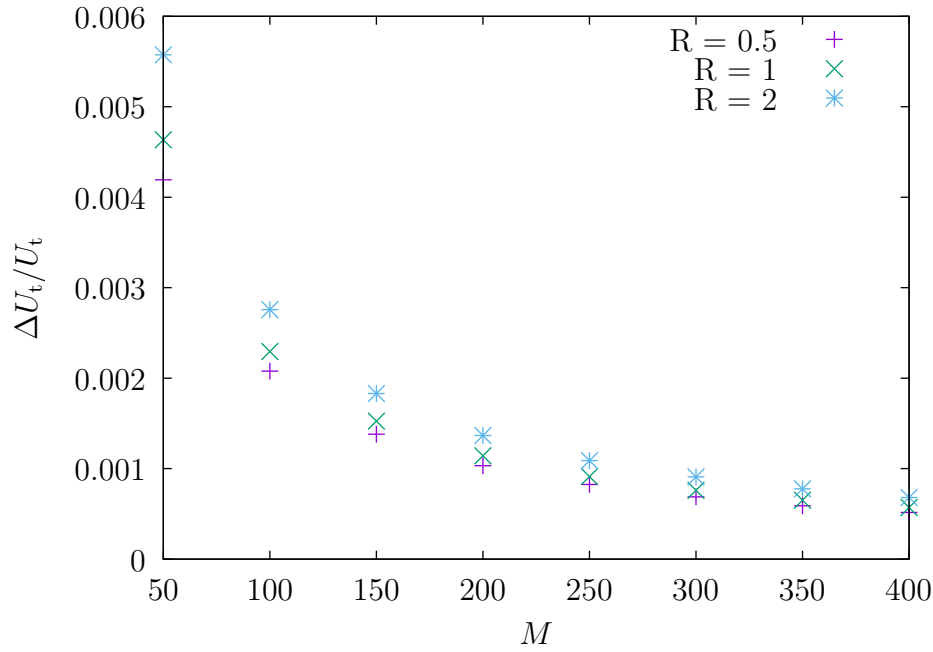
Figure 6: Plot showing the fractional error on the calculated terminal velocity of a spheroid in an infinite and uniform fluid as a function of the number of intervals used to discretise the particle surface. Results are shown for $R = 0.5$, 1 and 2. When 100 intervals are used, the fractional error is less than 0.003 and this decreases as the number of intervals increases. It can also be seen that as R increases so does the error.
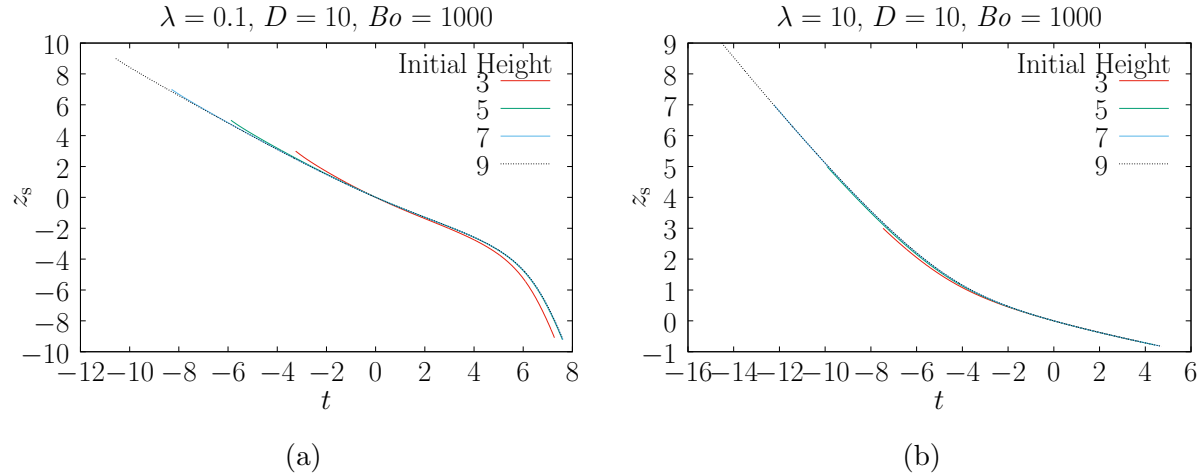
Figure 7: Plot of the vertical position of a sphere versus time for different initial sphere positions for $D = 10$ and $Bo = 1000$. a) $\lambda = 0.1$ - For initial positions greater or equal than 5 radii above the interface, the position curves quickly converge. b) $\lambda = 10$ - For initial positions greater or equal than 5 radii above the interface, the position curves are indistingusihable. For an initial position of 3, the curve quickly converges to the others.

5.2 Initial Height of Sphere

The interface will deform as the particle approaches and so we require the initial position of the particle to be far enough above the interface that the results are insensitive to the initial position. We tested the model for parameter values $R = 1$, $D = 10$, $Bo = 1000$ and both $\lambda = 0.1$ and $\lambda = 10$. Figure 7 shows the position of the sphere against time for the different viscosity ratios. The time $t = 0$ is defined as the moment when $z_\mathrm{s} = 0$. It is seen that the position curves converge for an initial position greater than or equal to 5 sphere radii above the interface. Figure 8 shows that the same is true when considering the volume of upper phase fluid entrained below the plane $z = 0$.

5.3 Truncation Length

The model is also tested for its sentitivity with respect to the radial coordinate $r = r_N$ at which the interface is truncated. Figure 9 shows the position of the sphere as a function
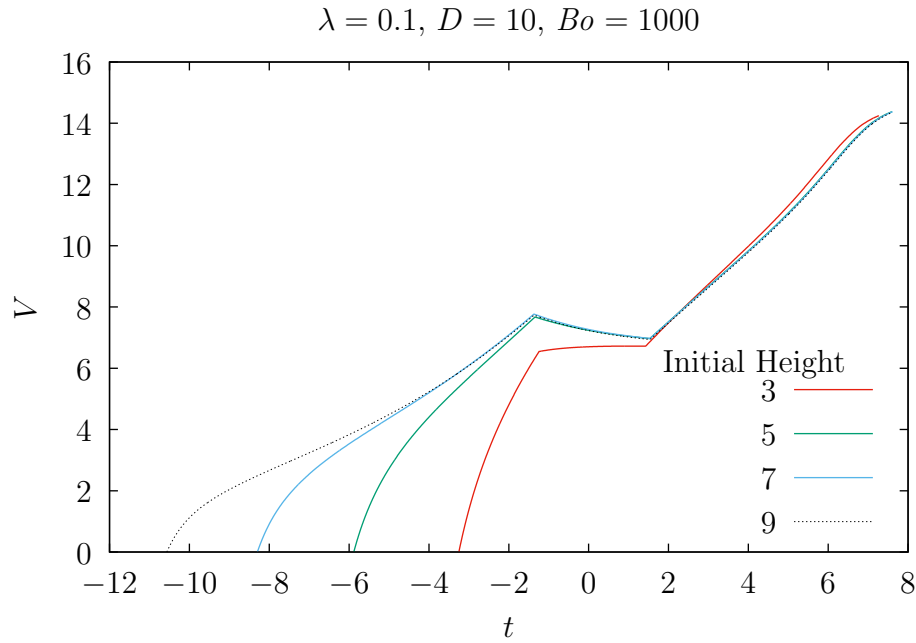
Figure 8: Curves showing the volume of upper phase fluid entrained below the plane $z = 0$ as a function of time, for different initial sphere positions and $D = 10$, $Bo = 1000$ and $\lambda = 0.1$. It is seen that the curves converge for an initial position greater than or equal to 5 sphere radii above the interface.
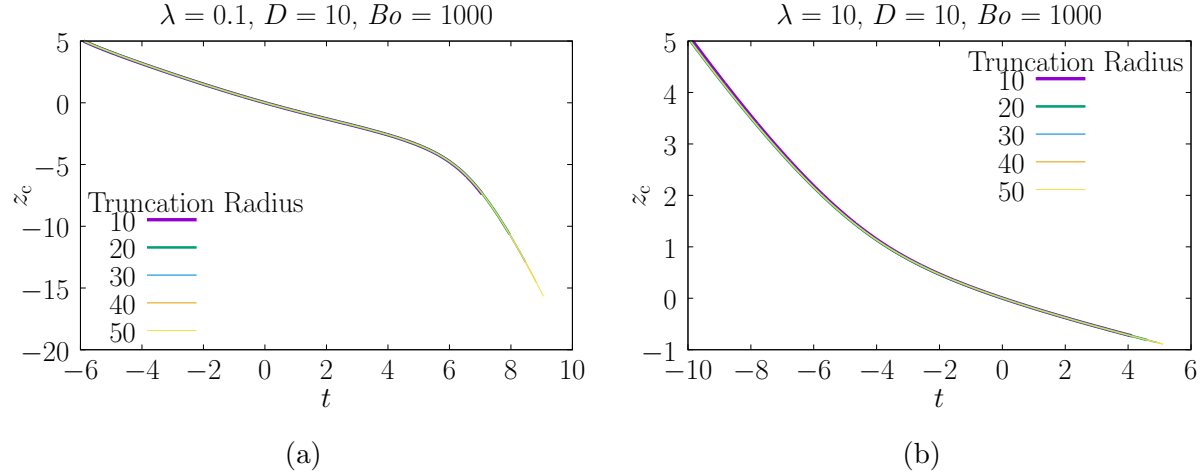
Figure 9: Plot of the vertical position of a sphere versus time for different truncation radii for $D = 10$, $Bo = 1000$ and both $\lambda = 0.1$ (a) and $\lambda = 10$ (b). The curves are identical for all truncation radii greater than or equal to 10.

of time for different r_N. It is seen that for $r_N \geq 10$ there is no change to the results. Figure 10 shows the dependence of the entrained volume as a function of time on the truncation radius. For $r_N \geq 20$ the curves are identical from the start of the simulation, and for $r_N = 10$ the curve converges to the others during the run.

5.4   Discretisation of Interface

The number of elements used to discretise the fluid interface N needs to be large enough that the model output is independent of N. Figure 11 shows the vertical position of the sphere as a function of time for different N. It can be seen that for $N \geq 50$ the curves are independent of N. However, the larger the value of N the longer the duration of the simulation. This is because larger values of N allow smaller separations between surfaces to be tolerated.

Figure 12 shows the effect of N on the time dependence of the volume of upper phase fluid entrained beneath the plane $z = 0$. As with the position curves, these are seen to be independent of N for $N \geq 50$.
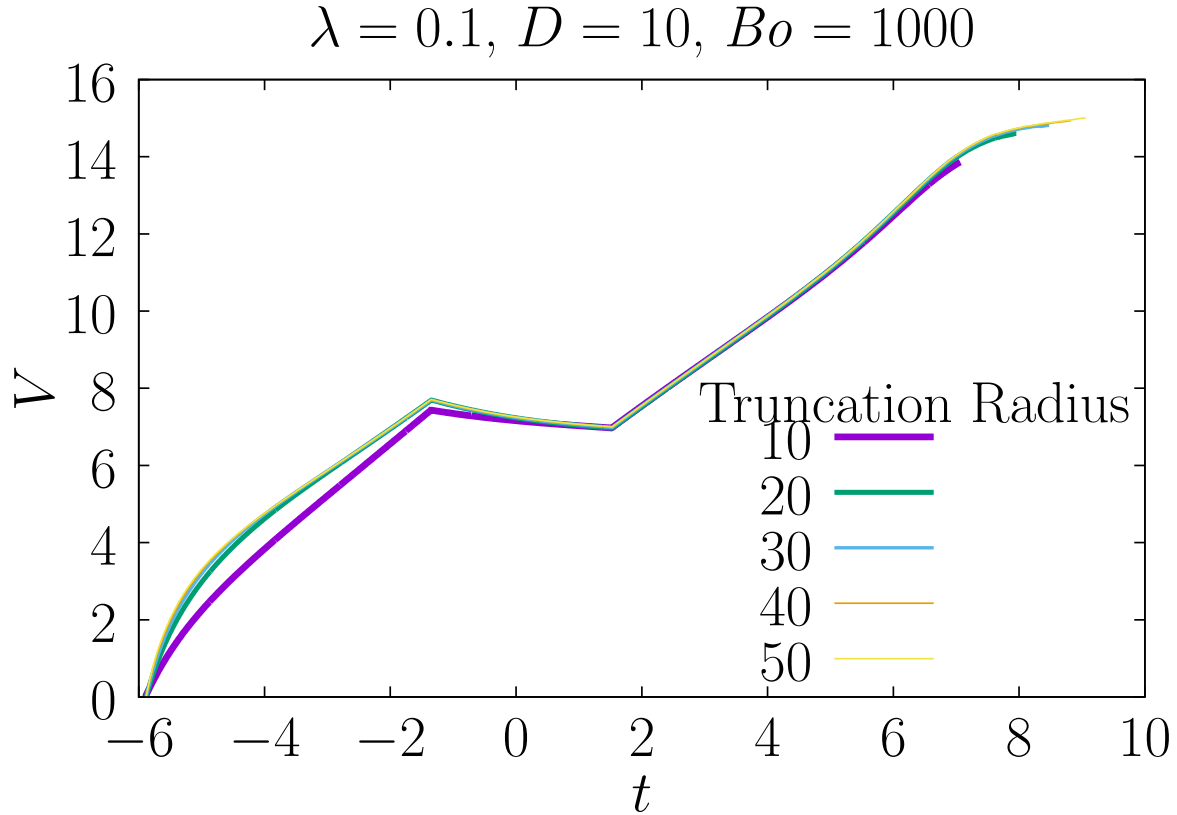
Figure 10: Curves showing the volume of upper phase fluid entrained below the plane $z = 0$ as a function of time, for different truncation radii and $D = 10$, $Bo = 1000$ and $\lambda = 0.1$. It is seen that the curves for $r_N \geq 20$ are identical from the start of the simulation, although the curve for $r_N = 10$ converges to the other curves during the run.
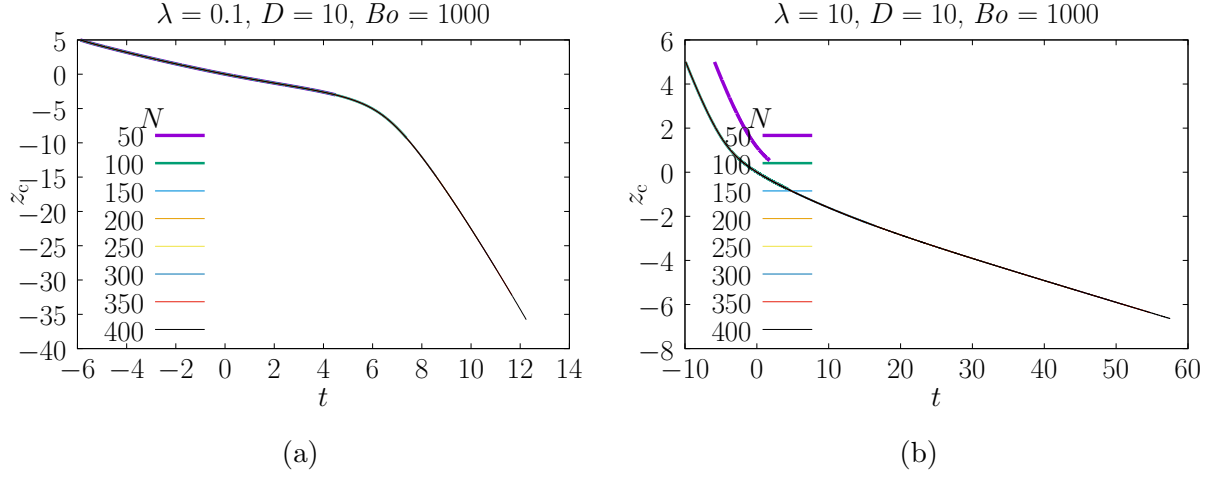
Figure 11: Vertical position of the sphere versus time for different numbers of elements used to discretise the interface N for $D = 10$, $Bo = 1000$ and both (a) $\lambda = 0.1$ and (b) $\lambda = 10$. The curves are identical for all choices of $N \geq 50$. However, the larger the value of N the longer the duration of the simulation.
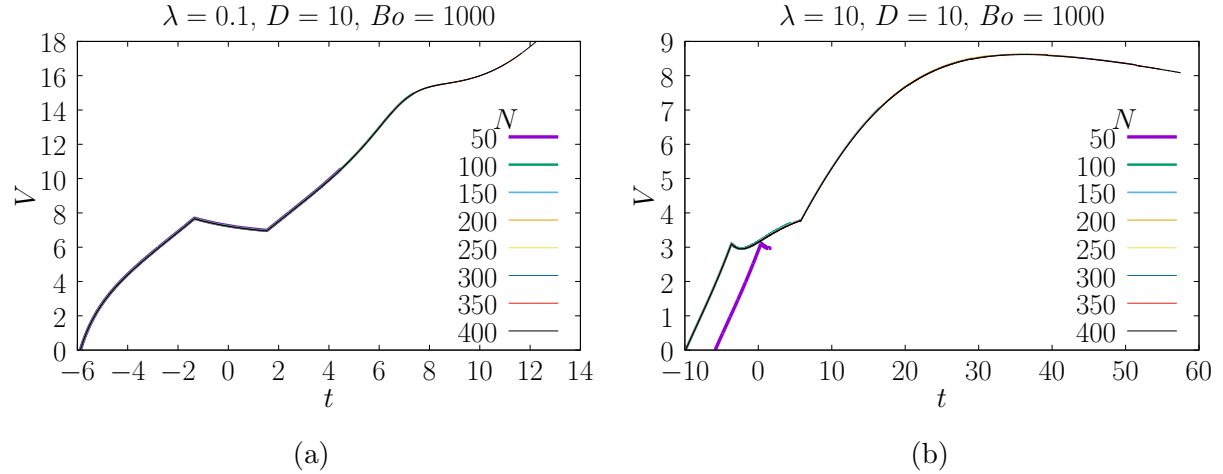

Figure 12: Volume of upper phase fluid entrained below the plane $z = 0$ as a function of time for different numbers of elements used to discretise the interface N for $D = 10$, $Bo = 1000$ and both (a) $\lambda = 0.1$ and (b) $\lambda = 10$. The curves are identical for all choices of $N \geq 50$.
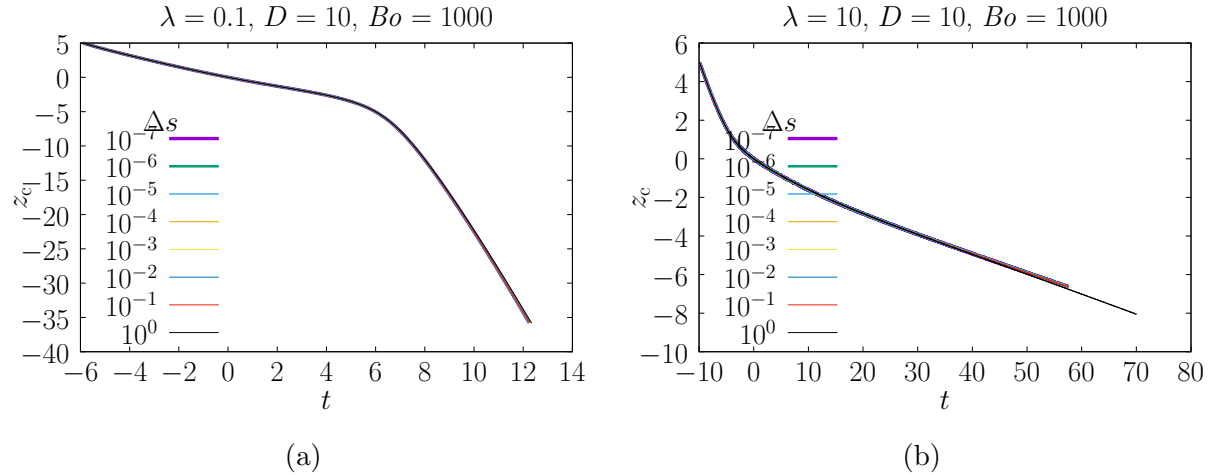
Figure 13: Vertical position of the sphere versus time for different values of the initial step size for numerical differentiation for $D = 10$, $Bo = 1000$ and both (a) $\lambda = 0.1$ and (b) $\lambda = 10$. The curves are identical for all choices of $\Delta s \leq 0.1$.

5.5   Numerical Differentiation of Interface

At each timestep it is necessary to differentiate the functions $r(s)$ and $z(s)$ that describe the interface as a function of arc-length (subsection 4.2). The numerical differentiation routines used require the choice of an initial step-size Δs (Press et al., 2007). The sensitivity of the model to this choice has been investigated and it is shown that results are independent of Δs for $\Delta s \leq 0.1$ (figures 13 and 14).
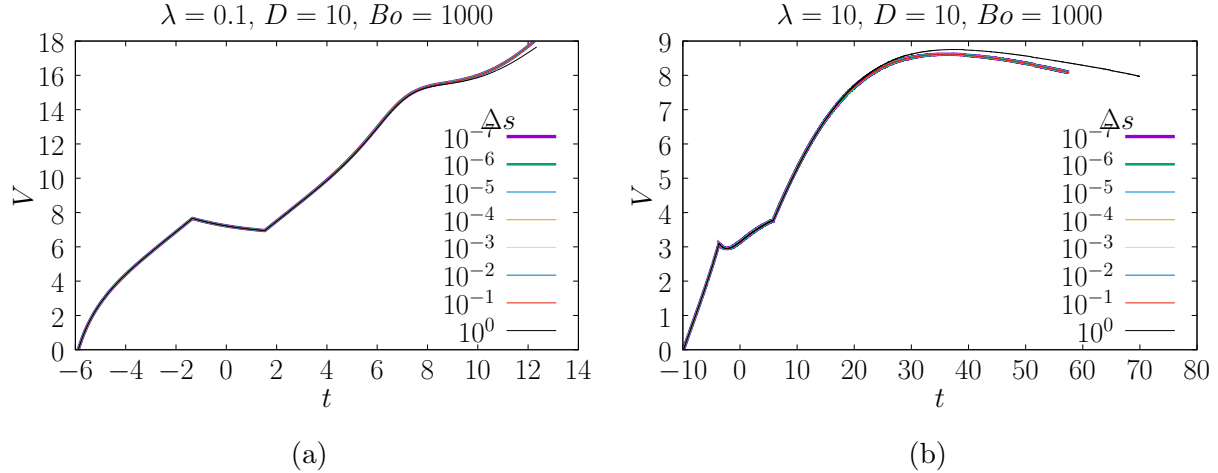
(a)   (b)

Figure 14: Time dependence of volume of upper phase fluid entrained below the plane $z = 0$ for different values of the initial step size for numerical differentiation for $D = 10$, $Bo = 1000$ and both (a) $\lambda = 0.1$ and (b) $\lambda = 10$. The curves are identical for all choices of $\Delta s \leq 0.1$.

5.6 Experimental Verification

6 Results

6.1 Settling Spheres

6.1.1 Floating versus Sinking

There are two possible situations for each simulation: floating or sinking. For simulations where floating is observed, the sphere velocity becomes negligibly small as the sphere-interface separation descreases, and never increases. This leads to the sphere attaining an equilibrium position at the interface (figures 15 and 16). Alternatively, the sphere velocity can remain significant at all times, and the interface deforms around the sphere as it sinks through the interface (figures 17 and 18).

A regime diagram has been constructed for the floating-sinking transition. It has been found that for $\lambda \leq 10$ the location of the transition in the parameter space defined by D,
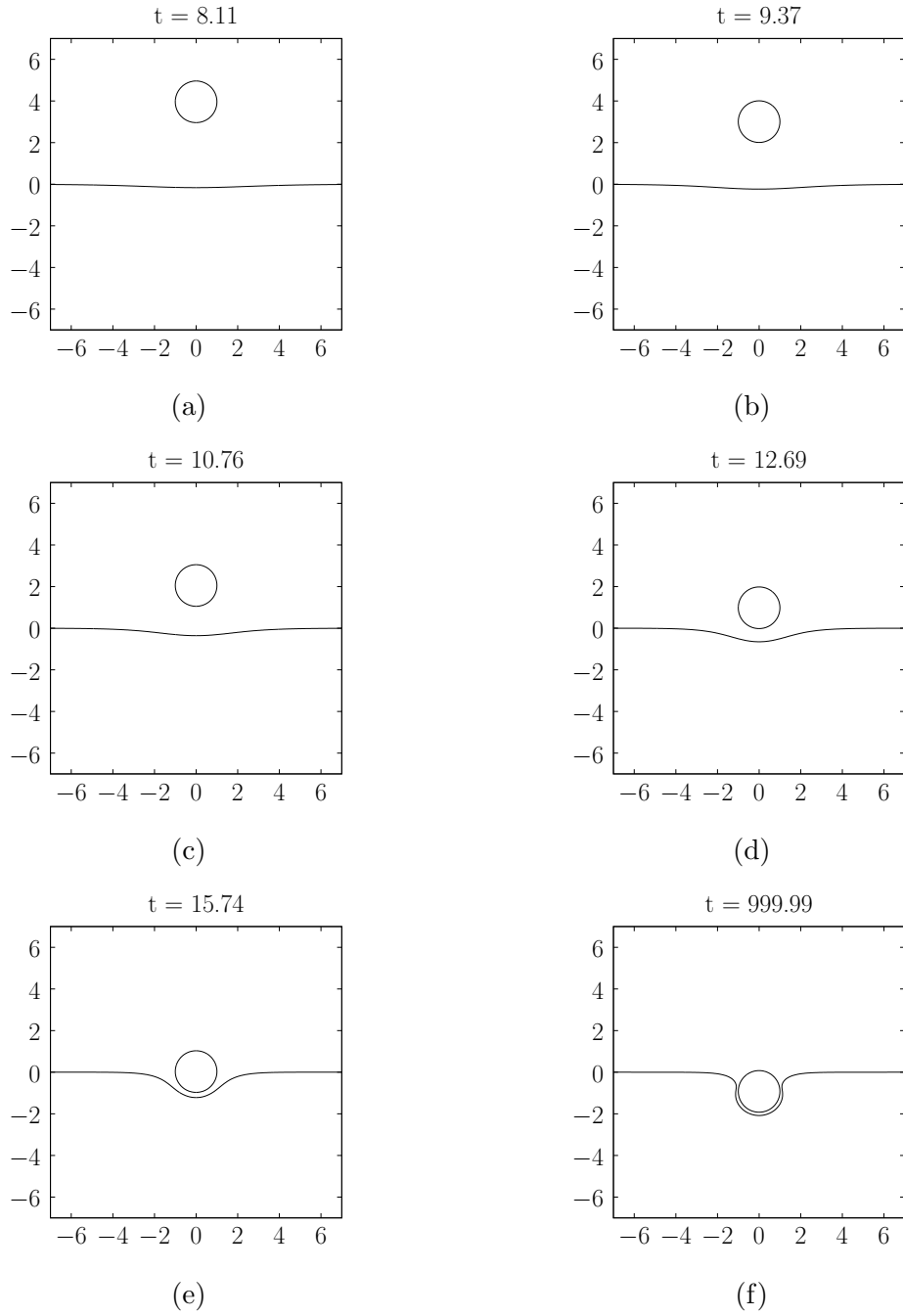
Figure 15: Settling of a sphere onto the interface when $D = 2.2$, $Bo = 2.5$ and $\lambda = 1$. The interface deforms as the sphere approaches and the sphere attains an equilibrium position with a thin film of fluid trapped between the sphere and the interface.
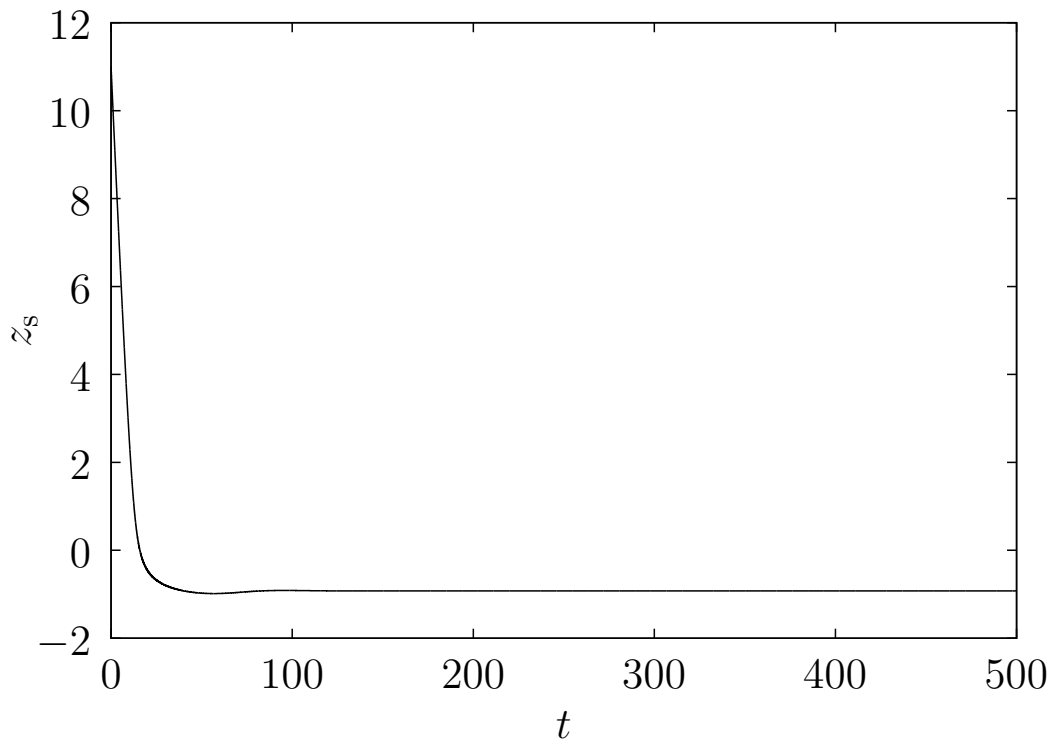
Figure 16: Position curve of the sphere, which is seen to attain an equilibrium position at the interface.
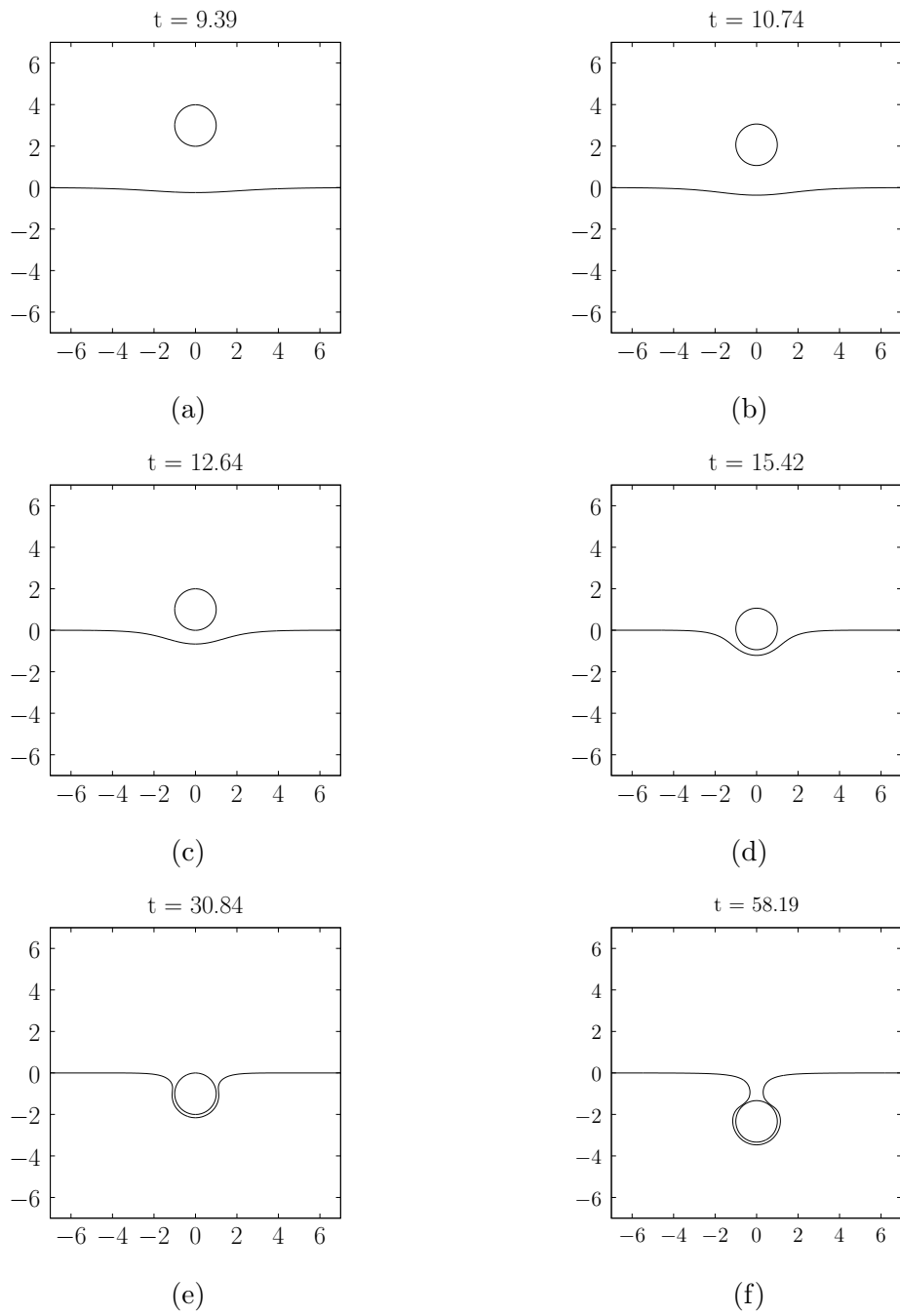
Figure 17: Settling of a sphere onto and through the interface when $D = 2.2$, $Bo = 3.5$ and $\lambda = 1$. The interface deforms as the sphere approaches and envelopes the sphere as it sinks.
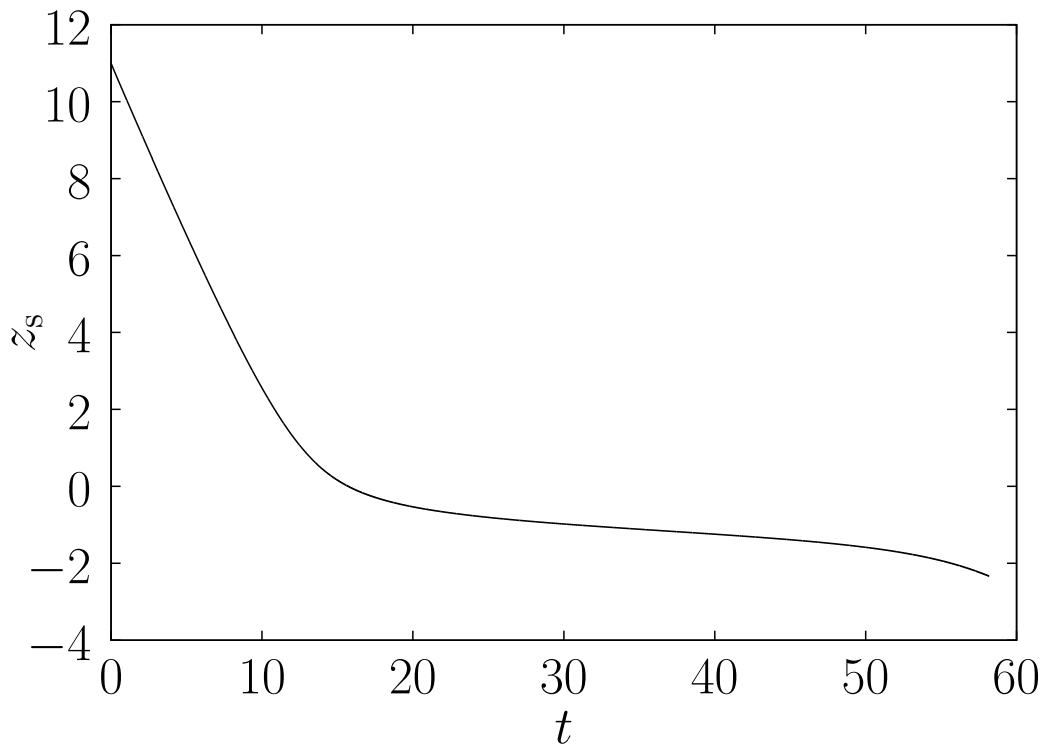
Figure 18: Position curve of the sphere, which is seen to slow down at the interface, before accelerating away.
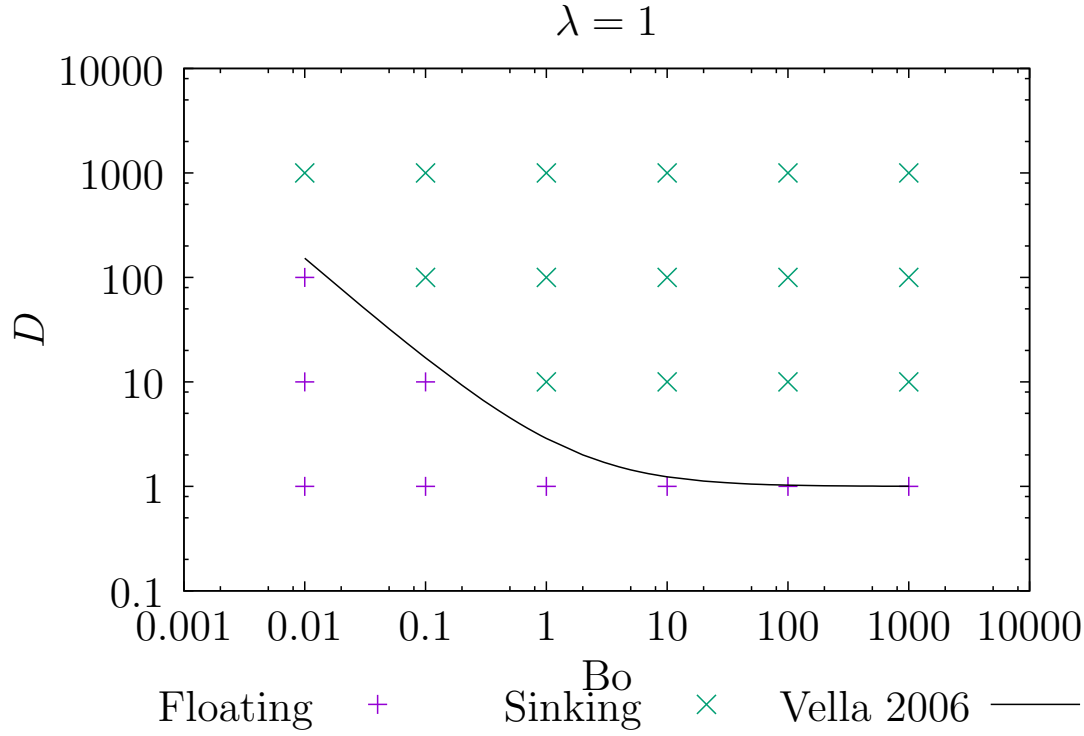
Figure 19: A regime diagram showing the fields of floating and sinking in the $\lambda = 1$ plane of the parameters space defined by λ, Bo, D. Points show results of simulations. Solid line shows prediction from theoretical model of (Vella et al., 2006).

Bo and λ is independent of λ. Figure 19 shows the transition in a plane of constant λ over orders of magnitude variation in D and Bo. Also shown is the prediction for this transition from the theoretical model of (Vella et al., 2006). This model finds the maximum D for a given Bo and contact angle for a sphere to be at equilibrium at an interface. This is different from our model, since no initial motion of the sphere is considered, and the existence of a contact line on the sphere is imposed. Despite these differences, we see that the results in figure 19 agree with this model. In figure 20 however, we show the results of a denser investigation of the paramter space, in the region where the transition curve has the highest curvature. It can be seen that although our model reproduces the shape of the predicted regime boundary, there is an offset such that our model predicts a higher maximum value of D for a given Bo.
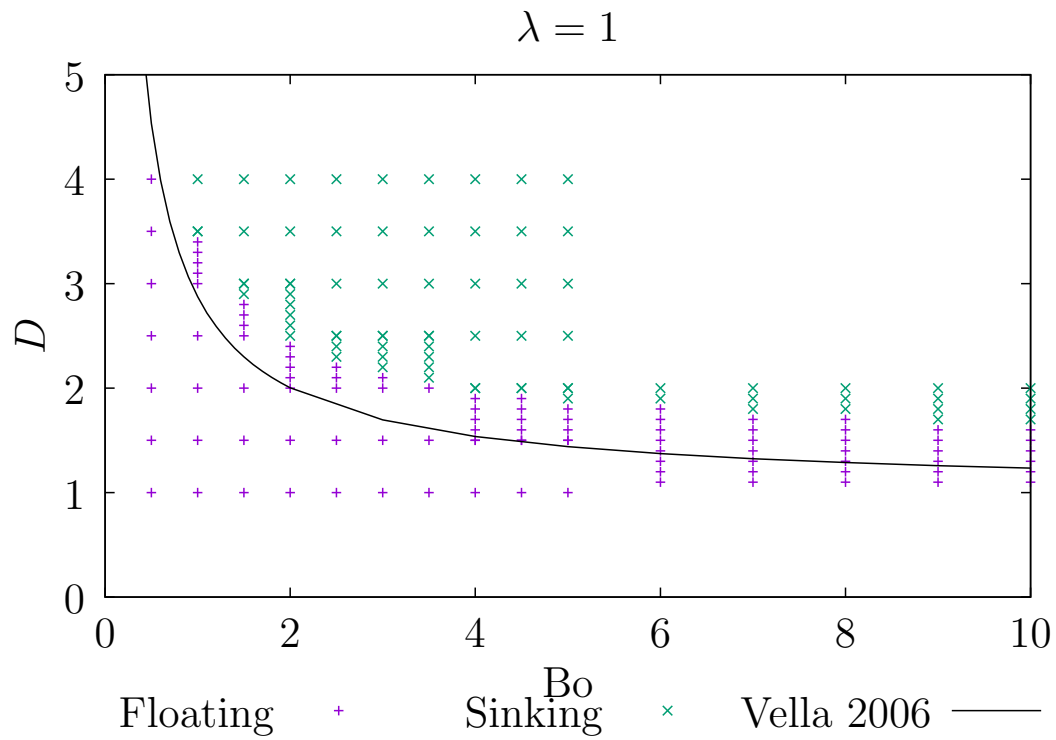
Figure 20: A regime diagram showing the fields of floating and sinking in the $\lambda = 1$ plane of the parameters space defined by λ, Bo, D. Points show results of simulations. Solid line shows prediction from theoretical model of (Vella et al., 2006).

6.1.2 Equilibrium Floating Position

For simulations where the sphere is observed to attain a static equilibrium position, the dependence of the final height of the sphere on D, Bo and λ has been determined.

6.1.3 Entrained Volume

6.2 Settling Spheroids

7 Discussion

7.1 Floating versus Sinking

Figure 20 shows the location of the floating and sinking regimes in the parameter space defined by Bo and D, as found using the BIM presented in sections 3 and 4. The curve in the figure shows the prediction for the transition between the two regimes found from the model of Vella et al. (2006) for a contact angle of π (sphere is completely wetted by upper fluid). It can be see that for a given Bo, the transition predicted by the BIM is found at a higher value of D than for the model presented by Vella et al. (2006). To rationalise this discrepancy, a brief description of the Vella et al. (2006) model is given here, highlighting the key differences with the BIM. Motivated by these differences, modifications are then proposed to the Vella et al. (2006) model and the validity of these is determined by comparing with the results from the BIM.

7.1.1 Vella et al. (2006) Model: A static description of the floating - sinking transition

The model proposed in Vella et al. (2006) considers the static problem of a sphere sitting at the interface between two immiscible, density stratified fluids. The presence of a three-

$\rho_{1(2)} =$ Density of fluid 1(2)
$\eta_{1(2)} =$ Dynamic viscosity of fluid 1(2)
$\sigma =$ Interfacial tension
$\rho_{S} =$ Density of sphere
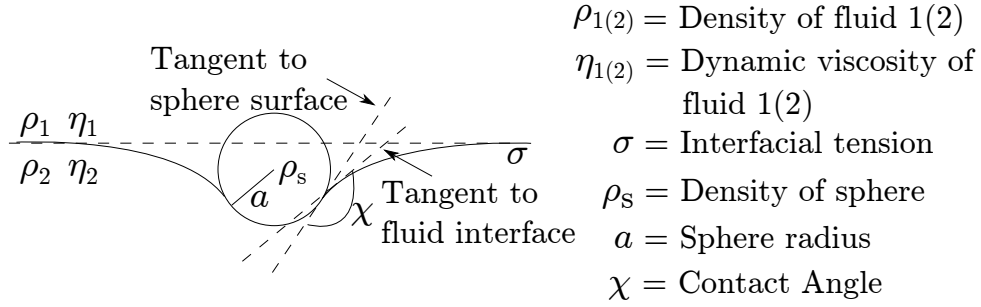$a =$ Sphere radius
$\chi =$ Contact Angle

Figure 21: The configuration of the problem as modelled by Vella et al. (2006). The key difference between this and the BIM presented in sections 3 and 4 is that this model is static, and a three phase contact line is assumed.

phase contact line is assumed. The configuration is as seen in figure 21. The model is a force balance of the surface tension, buoyancy and gravitational forces present in the system, and finds the condition for there to be an equilibrium position of the sphere at the interface.

In order to construct this model, it is neccessary to consider a result from Keller (1998); the vertical contribution of the IFT force on an object floating at an interface is equivalent to the buoyancy force of the fluid in the meniscus. This was first hypothesised by Galilei (Galilei, 1663; Vella, 2007). Figure 22 is a useful aid in explaining this. The volume of the meniscus is shown by the shaded regions external to the vertical cylindrical surface which contains the contact line. The IFT contribution to the vertical force is equal to the buoyancy of the upper fluid in this region. This means the force baclance for a sphere in equilibrium can be expressed as

$$\frac{4\pi(\rho_{s}-\rho_{1})a^{3}g}{3} = 2\pi a\sigma \sin\theta_{c} \sin(\chi-\theta_{c})+(\rho_{2}-\rho_{1})g\left(\frac{\pi a^{3}(2+3\cos\theta_{c}-\cos^{3}\theta_{c})}{3} - \pi z_{c}a^{2}\sin^{2}\theta_{c}\right)$$

(80)

where θ_{c} and z_{c} are the polar and vertical coordinates of the contact line respectively. The left hand side corresponds to the weight of the sphere relative to the weight of the same volume of the upper fluid. The right hand side is the sum of the IFT contribution (equivalent to the buoyant force due to the volume of the meniscus external to the contact
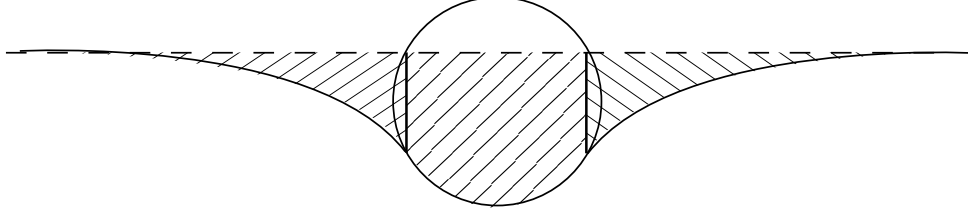
Figure 22: The different shadings show the regions internal and external to the meniscus.

line), and the displaced weight of the lower fluid relative to the upper fluid, in the volume of the meniscus internal to the contact line (central shaded region in figure 22).

Using the non-dimensionalisation scheme presented in section 3.1 the force balance can be written as

$$D = \frac{3}{4Bo}\left[2\sin\theta_c\sin(\chi - \theta_c) + Bo\left(-\frac{z_c'\sin^2\theta_c}{Bo^{1/2}} + \frac{2}{3} + \cos\theta_c - \frac{\cos\theta_c}{3}\right)\right].\qquad(81)$$

For a given Bo, contact angle χ and contact line position (given by θ_c and z_c'), this equation gives the largest possible value of D for which an equilibrium floating position exists. The contact line position itself is found by solving the Laplace-Young equation for the interfacial profile subject to the boundary condition given by the contact angle condition on the sphere, and imposing that the interface returns to its equilibrium position away from the sphere. This is a boundary value problem (Riley et al., 2006) and has no analytical solution in an axisymmetric geometry so needs to be solved numerically.

Hence, the routine for finding the maximum D at which floating can occur for a given Bo and χ is found by sweeping over different values of θ_c between 0 and π and solving the Laplace-Young equation for the corresponding height of the contact line z_c for each case. These are then substituted into equation 81. The largest value of D calculated in

the sweep is the largest value of D for which floating is possible for a given Bo and χ. The curve shown in figure 20 is the predicted floating-sinking transition for $\chi = pi$.

7.1.2   Difference between the static and BIM models

To explain the discrepancy between the two models in their prediction of the floating-sinking transition location in the Bo-D parameters space, it is important to consider the differences between the models. The static model, as suggested by its name, is static. It merely considers the conditions at which a sphere can be in equilibrium at an interface, given a contact line exists. It doesn't account for any prior motion of the sphere. It has been shown for cylinders and a liquid-gas interface that increasing the speed of impact reduces the maximum density and/or size of cylinder that can float at the interface Vella and Metcalfe (2007); Vella and Li (2010). This situation is theoretically considered by using an initial condition of the cylinder being in contact with the interface but having some initial velocity. It is important to note that in these studies the flow is in the inertial regime.

The key difference with the BIM used in this study is that in the initial state of the system the sphere is multiple radii above the interface and is settling at its terminal velocity. Hence, as well as having an initial velocity, no contact line exists. Since there is a no-slip boundary condition on the surface of the sphere (equation 50), the fluid immediately adjacent to the sphere will never be displaced. This means that there will always remain a layer of upper phase fluid between the sphere and the interface. Hence it is impossible to reproduce the film drainage mode as seen in the experimental study. The presence of this layer will also have an effect on the floating-sinking transition, since it is effectively provides an extra contribution to the upward buoyancy forces.

For a given Bo, the BIM predicts the value of D at which the floating-sinking transition occurs to be positively displaced relative to the prediction from the static model. This suggests that the effect of the trapped layer of upper phase fluid between the sphere and the interface has a more significant effect than the impact of the sphere.
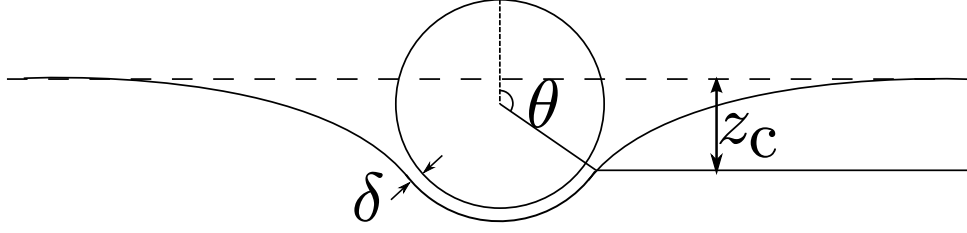
Figure 23: The modified static model configuration. The sphere and the interface are separated by a film of upper phase fluid of constant thickness δ.

7.1.3   Modified static model

Motivated by the observation that the trapped layer has a greater effect on the floating-sinking transition than the impact of the sphere, a static model, modified from that described in section 7.1.1, is presented here which accounts for a trapped layer of upper phase fluid (figure 23). For simplicity, this layer is assumed to have a uniform thickness. Hence, in this model, the interface can be described by two parts. The first is a spherical cap of radius $a + \delta$ concentric with the sphere. At some polar angle θ_c this transitions into a meniscus whose geometry is determined by the Laplace-Young equation subject to the condition that at $\theta = \theta_c$, the tangent planes to both the spherical cap and the meniscus are coincident.

The force balance for this geometry can be realised by modifying equation 80 by replacing all the occurences of a on the right-hand side by $a + \delta$ and setting $\chi = \pi$;

$$\frac{4\pi(\rho_s - \rho_1)a^3 g}{3} = 2\pi(a+\delta)\sigma\sin^2\theta_c + (\rho_2 - \rho_1)g\left(\frac{\pi(a+\delta)^3(2 + 3\cos\theta_c - \cos^3\theta_c)}{3} - \pi z_c(a+\delta)^2\sin^2\theta_c\right).$$

(82)

As in section 7.1.1, this can be non dimensionalised to give

$$D = \frac{3\Delta^{1/2}}{4Bo}\left[2\sin^2\theta_c + Bo\Delta\left(-\frac{z_c'\sin^2\theta_c}{Bo^{1/2}\Delta^{1/2}} + \frac{2}{3} + \cos\theta_c - \frac{\cos^3\theta_c}{3}\right)\right], \qquad (83)$$
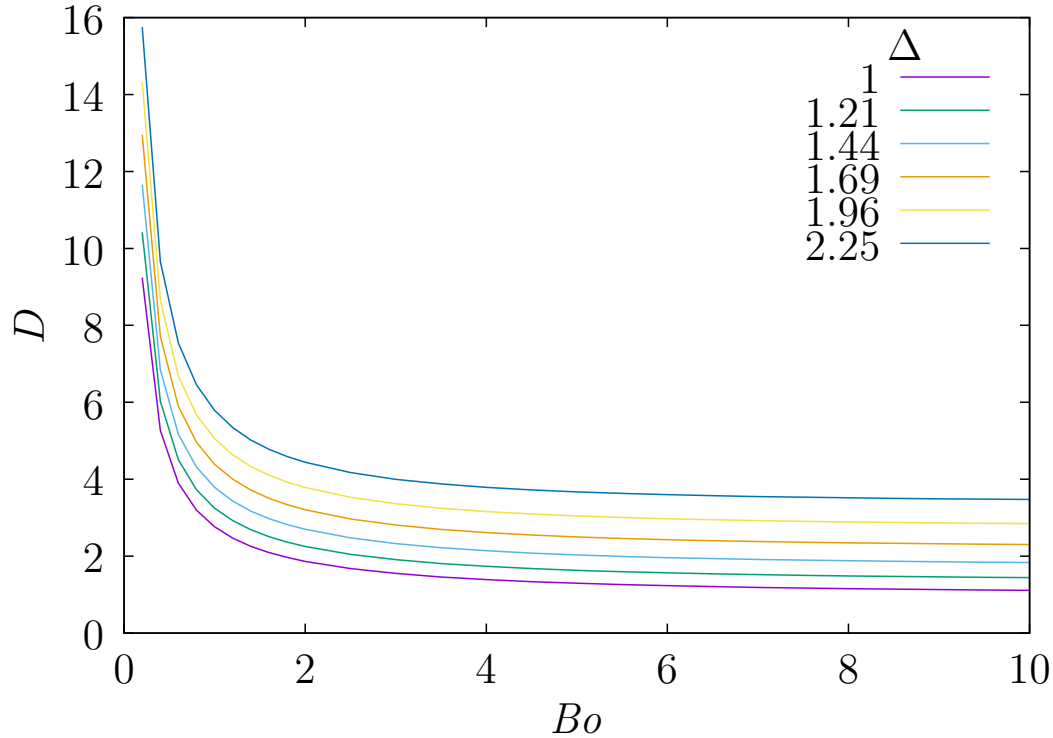
Figure 24: Plots of equation 83 for different values of Δ. As Δ increases the floating-sinking transition at a given value of Bo shifts to higher values of D.

where

$$\Delta = \left(1 + \frac{\delta}{a}\right)^2. \tag{84}$$

For a given Bo, θ_c and Δ, equation 83 gives the maximum value of D for which a sphere is in equilibrium whilst separated from an interface by a film of thickness δ. Using a routine similar to that described in section 7.1.1 the floating-sinking transition in the Bo-D space for different δ can be found (figure 24). It can be seen that increasing the value of Δ. and so the relative thickness of the trapped film, it is possible to support denser and larger spheres at a fluid interface. This is intuitively explained by the additional contribution of the buoyant fluid in the film to the upward force.

7.1.4   Comparison with BIM results

To test if the modified static model provides a suitable explanation for the observed floating-sinking transition in the BIM results, the results of four simulations where floating was observed but the parameters are close to the transition were chosen for further analysis (see table 2). For each of these simulations, the final profile of the thickness of the film separating the sphere from the interface was considered (figure 25) and the mean thickness of the film, weighted by the radial coordinate of the fluid, was calculated (given in table 2).

Table 2: BIM simulations chosen for comparison with the modified static model, and the mean final thickness of the film separating the sphere from the interface.

D	Bo	$\bar{\delta}$	Δ
3.4	1.0	0.175	1.381
2.8	1.5	0.171	1.371
2.2	2.5	0.160	1.346
2.0	3.5	0.157	1.339

As can be seen in figures 26a to 26d, the film is seen to contract at its periphery. This agrees with previous experimental observations (Hartland, 1968) where it has been noted that the film constricts at it's periphery, just inside the point where it transitions to the meniscus profile. This constriction is predicted by the theoretical model of (Jones and Wilson, 1978) as a consequence of pressure gradients in the film as a consequence of the change in curvature of the interface at the film periphery.

Additionally, the point where the film transitions to the meniscus occurs at a polar angle of $\theta \approx \pi/2$. This is the first point of agreement with the modified static model. Differentiating of equation 83 with respect to θ_c and setting $\partial D/\partial \theta_c = 0$ gives a solution of $\theta_c = \pi/2$ (other solutions may exist but cannot be extracted due to the unavailability for a closed expression for $\partial z_c/\partial \theta_c$). Hence, there is a (at least a local) maximum in maximum value of D for which floating can occur at $\theta_c = \pi/2$. Since the chosen simulations are close to the transition, it is to be expected that they have an equilibrium configuration
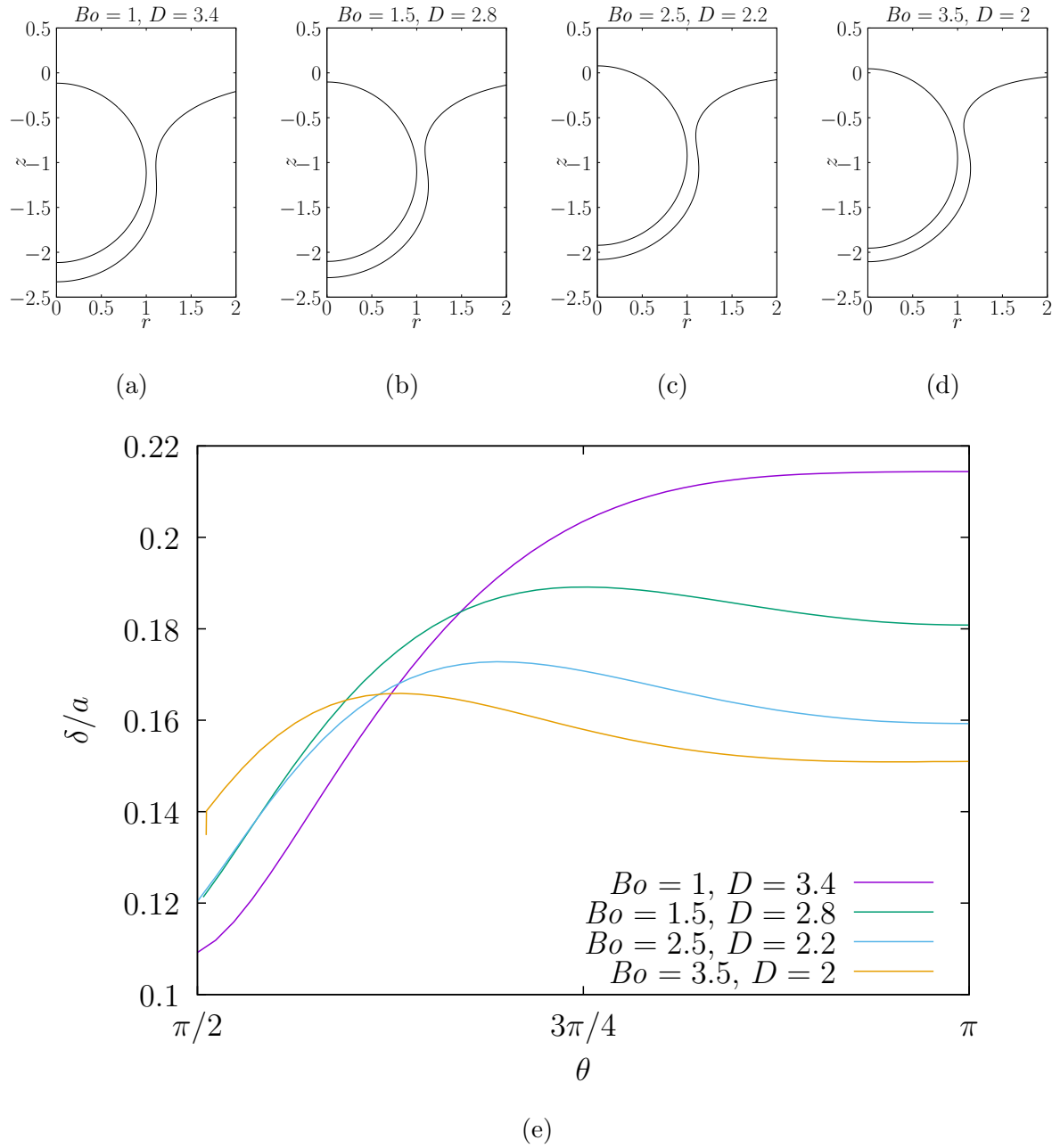
Figure 25: a) to d) The final equilibrium configuration of the simulations listed in table 2. In each example, the film constricts at approximately $\theta = \pi/2$, just before the interface transitions into the meniscus profile. e) Film thickness as a function of θ. The film thickness can be seen to vary up to about 50%.

which gives this maximum upward force.

Figure 25e shows the film thickness as a function of θ for the different simulations. It can be seen that, unlike in the modified static model, the film has a variable thickness which can vary by up to 50%. Therefore, to compare these simulations with the results from the static model, the mean thickness of the film, weighted by the radial coordinate, has been calculated. The reason for weighting by the radial coordinate is because the axisymmtric geometry means, for a given film thickness, there is a greater volume of fluid at a larger radius. The weighted mean thicknesses $\bar{\delta}$ and their corresponding value of Δ are given in table 2. Figure 26 shows the predicted transitions for these values of Δ compared to the results from the BIM. It can be seen that all values of Δ reproduce the observed transition for $Bo \geq 4$ and that as Δ decreases then the lowest value of Bo at which there is agreement becomes smaller; for $\Delta = 1.339$ there is agreement for $Bo \geq 1.5$. For smaller Bo, the static model predicts the transition to be at larger values of D than the BIM model. This discrepancy is most likely explained by the fact that as Bo decreases, the amount of variation in film thickness increases (figure 25e) so the assumption of constant film thickness in the static model begins to no longer be valid. However, regardless, the modified static model still does a very good job of predicting the transition observed in the BIM, compared to the original static model (see figure 20).

A   Dirac Delta Function

In a volume $\mathcal{V}$ bounded by a surface $\mathcal{S}$, the Dirac delta function $\delta(\boldsymbol{x} - \boldsymbol{y})$ is defined as (Riley et al., 2006)

$$\int_{\mathcal{V}} f(\boldsymbol{y})\delta(\boldsymbol{x} - \boldsymbol{y})\mathrm{d}^3\boldsymbol{y} = \begin{cases} f(\boldsymbol{x}), & \boldsymbol{x} \in \mathcal{V} \\ \frac{f(\boldsymbol{x})}{2}, & \boldsymbol{x} \in \mathcal{S} \\ 0, & \text{otherwise} \end{cases} . \tag{85}$$

The result for $\boldsymbol{x} \in \mathcal{S}$ is only valied for the case that the surface is Lyapunov smooth (a
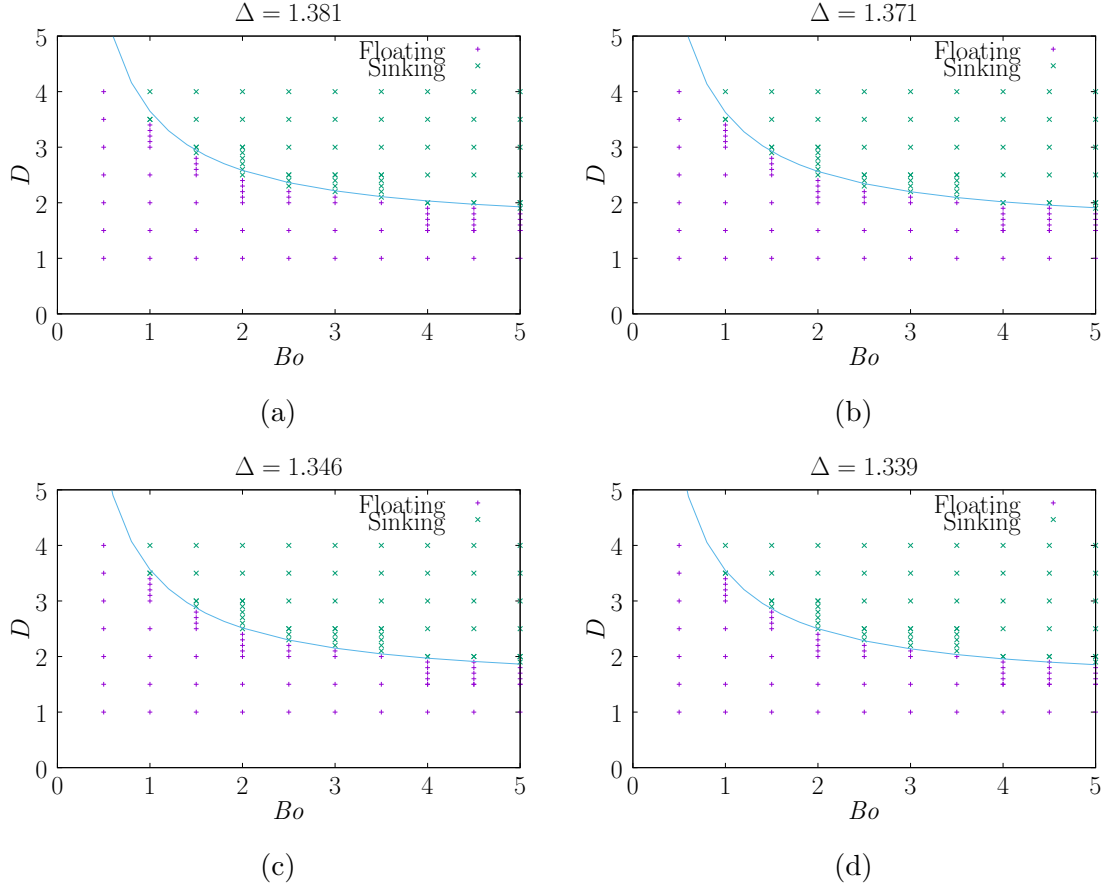
Figure 26: Predicted transitions based on the mean thickness of each film.

local tangent plane exists everywhere) (Gunter, 1967). Equation 85 means that

$$\int_{\mathcal{V}} \delta(\boldsymbol{x} - \boldsymbol{y})\mathrm{d}^3\boldsymbol{y} = 1, \quad \boldsymbol{x} \in \mathcal{V}. \tag{86}$$

A key property of the delta function is that it is symmetric under a change of sign of the argument;

$$\delta(-\boldsymbol{x}) = \delta(\boldsymbol{x}). \tag{87}$$

It also needs to be noted that the Dirac delta function can be expressed as (Riley et al., 2006)

$$\delta(\boldsymbol{\xi}) = \frac{1}{(2\pi)^3} \int \mathrm{e}^{i\boldsymbol{k}\cdot\boldsymbol{\xi}}\mathrm{d}^3\boldsymbol{k}, \tag{88}$$

where $\boldsymbol{k}$ is the transform variable and i is the imaginary unit.

B   Greens Functions for Stokes Flow

We present here a derivation of equations 31 and 32 following Ladyzhenskaya (1963). First, the Greens function for dynamic pressure $\hat{P}(\boldsymbol{\xi})$ is defined such that

$$\hat{T}_{ij}(\boldsymbol{\xi}) = -\hat{P}(\boldsymbol{\xi})\delta_{ij} + \Lambda[\partial_i'\hat{u}_j(\boldsymbol{\xi}) + \partial_j'\hat{u}_i(\boldsymbol{\xi})]. \tag{89}$$

Substituting this into equation 30, and using equation 29 yields

$$-\partial_j'\hat{P}(\boldsymbol{\xi}) + \Lambda\partial_i'\partial_i'\hat{u}_j(\boldsymbol{\xi}) + \mathcal{F}_j\delta(\boldsymbol{\xi}) = 0. \tag{90}$$

We also define two further quantities, $\bar{P}_i$ and $\bar{u}_{ij}$ such that

$$\hat{P}(\boldsymbol{\xi}) = \mathcal{F}_i \bar{P}_i(\boldsymbol{\xi}), \tag{91}$$

and

$$\hat{u}_j(\boldsymbol{\xi}) = \mathcal{F}_i \bar{u}_{ij}(\boldsymbol{\xi}). \tag{92}$$

Substitution of these expressions into equations 29 and 90, and rearranging results in

$$\partial'_i \bar{u}_{ij}(\boldsymbol{\xi}) = 0, \tag{93}$$

and

$$-\partial'_j \bar{P}_i(\boldsymbol{\xi}) + \Lambda \partial'_k \partial'_k \bar{u}_{ij}(\boldsymbol{\xi}) + \delta_{ij}\delta(\boldsymbol{\xi}) = 0. \tag{94}$$

To derive functional forms for the Greens functions, it is necessary to express equations 93 and 94 in Fourier representation. To do this we need to define the Fourier transformed variables $\tilde{P}_{\alpha,i}$ and $\tilde{u}_{\alpha,ij}$ (Riley et al., 2006):

$$\bar{P}_i(\boldsymbol{\xi}) = \frac{1}{(2\pi)^{3/2}} \int \tilde{P}_i(\boldsymbol{k}) \mathrm{e}^{i\boldsymbol{k}\cdot\boldsymbol{\xi}} \mathrm{d}^3\boldsymbol{k}, \tag{95}$$

and

$$\bar{u}_{ij}(\boldsymbol{\xi}) = \frac{1}{(2\pi)^{3/2}} \int \tilde{u}_{ij}(\boldsymbol{k}) \mathrm{e}^{i\boldsymbol{k}\cdot\boldsymbol{\xi}} \mathrm{d}^3\boldsymbol{k}. \tag{96}$$

where $\boldsymbol{k}$ is the transform variable, and i is the unit imaginary number. Substitution of these, and the Fourier definition of the Dirac delta function (equation 88 in appendix A)

into equations 93 and 94 gives the Fourier representations of the continuity and Stokes equations respectively. Following some manipulation these can be written as

$$k_i \tilde{u}_{ij}(\boldsymbol{k}) = 0, \tag{97}$$

and

$$-ik_j \tilde{P}_i(\boldsymbol{k}) - \Lambda k^2 \tilde{u}_{ij}(\boldsymbol{k}) + \frac{\delta_{ij}}{(2\pi)^{3/2}} = 0. \tag{98}$$

where $k = k_i k_i$. By contracting equation 98 with k_j, substituting in equation 97, and rearranging, it is then possible to obtain the Fourier representation of the Greens function for pressure;

$$\tilde{P}_i(\boldsymbol{k}) = \frac{-ik_i}{(2\pi)^{3/2} k^2}. \tag{99}$$

A final substitution of this into equation 95 gives the Greens function for pressure;

$$\bar{P}_i(\boldsymbol{\xi}) = \frac{-i}{(2\pi)^3} \int \frac{k_i e^{i\boldsymbol{k} \cdot \boldsymbol{\xi}} \mathrm{d}^3 \boldsymbol{k}}{k^2}. \tag{100}$$

This integral is evaluated in appendix B.1 and it is shown that

$$\bar{P}_i(\boldsymbol{\xi}) = -\frac{1}{4\pi} \partial_i' \left(\frac{1}{\xi} \right) = \frac{\xi_i}{4\pi \xi^3} \quad , \quad \xi = \xi_i \xi_i. \tag{101}$$

We also need to find an equivalent expression for $\bar{u}_{ij}$. To do so, substitute equation 99 into equation 98 and rearrange;

$$\tilde{u}_{ij}(\boldsymbol{k}) = \frac{k^2 \delta_{ij} - k_i k_j}{(2\pi)^{3/2} k^4 \Lambda}. \tag{102}$$

Combining this with equation 96 results in an expression for the Greens function for velocity;

$$\bar{u}_{ij}(\boldsymbol{\xi}) = \frac{1}{(2\pi)^3\Lambda}\left(\delta_{ij}\int\frac{\mathrm{e}^{i\boldsymbol{k}\cdot\boldsymbol{\xi}}\mathrm{d}^3\boldsymbol{k}}{k^2} - \int\frac{k_ik_j\mathrm{e}^{i\boldsymbol{k}\cdot\boldsymbol{\xi}}\mathrm{d}^3\boldsymbol{k}}{k^4}\right). \tag{103}$$

These integrals are evaluated in appendix B.2 (equations 117 and 123) and following some manipulation we find

$$\bar{u}_{ij}(\boldsymbol{\xi}) = \frac{1}{8\pi\Lambda\xi}\left(\delta_{ij} + \frac{\xi_i\xi_j}{\xi^2}\right). \tag{104}$$

We can now substitute equations 101 and 104 into 91 and 92 to obtain

$$\hat{P}(\boldsymbol{\xi}) = \frac{\mathcal{F}_i\xi_i}{4\pi\xi^3}, \tag{105}$$

and

$$\hat{u}_j(\boldsymbol{\xi}) = \frac{\mathcal{F}_i}{8\pi\Lambda_\alpha\xi}\left(\delta_{ij} + \frac{\xi_i\xi_j}{\xi^2}\right). \tag{106}$$

Substitution of equations 105 and 106 into equation 89 results in

$$\hat{T}_{ij}(\boldsymbol{\xi}) = \frac{-3\mathcal{F}_k\xi_i\xi_j\xi_k}{4\pi\xi^5}. \tag{107}$$

The kernels J_{ij} and K_{ijk} are defined as

$$J_{ij} = \frac{1}{8\pi\xi}\left(\delta_{ij} + \frac{\xi_i\xi_j}{\xi^2}\right), \tag{108}$$

and

$$K_{ijk} = \frac{-3\xi_i\xi_j\xi_k}{4\pi\xi^5}. \tag{109}$$

Hence we obtain the Greens functions for the velocity and stress fields (equations 31 and 32). Note that under the interchange $\boldsymbol{\xi} \to -\boldsymbol{\xi}$ the kernels are symmetric and anti-symmetric respectively;

$$J_{ki}(-\boldsymbol{\xi}) = J_{ki}(\boldsymbol{\xi}), \tag{110}$$

$$K_{jik}(-\boldsymbol{\xi}) = -K_{jik}(\boldsymbol{\xi}). \tag{111}$$

B.1   Integral for Greens Function for Pressure

Here we present a proof of the evaluation of the integral in equation 100. First recall the identity (Jackson, 1999; Frahm, 1982)

$$\partial_i\partial_i\left(\frac{1}{\xi}\right) = -4\pi\delta(\boldsymbol{\xi}). \tag{112}$$

Substituting in the Fourier definition of the delta function (equation 88) leads to

$$\partial_i\partial_i\left(\frac{1}{\xi}\right) = \frac{-4\pi}{(2\pi)^3}\int e^{i\boldsymbol{k}\cdot\boldsymbol{\xi}}\mathrm{d}^3\boldsymbol{k}. \tag{113}$$

Inspection of this then suggests

$$\partial_i\left(\frac{1}{\xi}\right) = \frac{4i\pi}{(2\pi)^3}\int \frac{k_i e^{i\boldsymbol{k}\cdot\boldsymbol{\xi}}\mathrm{d}^3\boldsymbol{k}}{k^2}. \tag{114}$$

Hence

$$\frac{-i}{(2\pi)^3} \int \frac{k_i e^{i\boldsymbol{k}\cdot\boldsymbol{\xi}} \mathrm{d}^3\boldsymbol{k}}{k^2} = -\frac{1}{4\pi} \partial_i \left(\frac{1}{\xi}\right). \tag{115}$$

B.2 Integrals for the Greens Function for Velocity

Here we present proofs of the evaluation of the two integrals in equation 103. For the first integral, inspection of equation 114 in appendix B.1 shows

$$\frac{1}{\xi} = \frac{4\pi}{(2\pi)^3} \int \frac{e^{i\boldsymbol{k}\cdot\boldsymbol{\xi}} \mathrm{d}^3\boldsymbol{k}}{k^2}. \tag{116}$$

Hence the fist integral in equation 103 is

$$\int \frac{e^{i\boldsymbol{k}\cdot\boldsymbol{\xi}} \mathrm{d}^3\boldsymbol{k}}{k^2} = \frac{(2\pi)^3}{4\pi\xi}. \tag{117}$$

The second integral requires a bit more work. Firstly, express it in a different form;

$$\int \frac{k_i k_j e^{i\boldsymbol{k}\cdot\boldsymbol{\xi}} \mathrm{d}^3\boldsymbol{k}}{k^4} = \partial_i \partial_j \left(\int \frac{e^{i\boldsymbol{k}\cdot\boldsymbol{\xi}} \mathrm{d}^3\boldsymbol{k}}{k^4}\right). \tag{118}$$

To evalaute this, first consider $\nabla^4\xi = \nabla^2(\nabla^2\xi)$. Expanding ∇^2 in spherical polar coordinates centred on $\xi = 0$ shows

$$\nabla^4\xi = 2\nabla^2\left(\frac{1}{\xi}\right). \tag{119}$$

Combining this with equation 113 we obtain

$$\nabla^4\xi = \frac{-8\pi}{(2\pi)^3} \int e^{i\boldsymbol{k}\cdot\boldsymbol{\xi}} \mathrm{d}^3\boldsymbol{k}. \tag{120}$$

Insepection of this yields

$$\xi = \frac{-8\pi}{(2\pi)^3} \int \frac{e^{i\boldsymbol{k}\cdot\boldsymbol{\xi}} d^3\boldsymbol{k}}{k^4}. \tag{121}$$

Rearranging this produces an expression for the integral on the right hand side of equation 118;

$$\int \frac{e^{i\boldsymbol{k}\cdot\boldsymbol{\xi}} d^3\boldsymbol{k}}{k^4} = -\frac{(2\pi)^3 \xi}{8\pi}. \tag{122}$$

Hence

$$\int \frac{k_i k_j e^{i\boldsymbol{k}\cdot\boldsymbol{\xi}} d^3\boldsymbol{k}}{k^4} = \frac{(2\pi)^3 \partial_i' \partial_j' \xi}{8\pi}. \tag{123}$$

C   Lorentz Reciprocal Theorem

Consider a pair of velocity fields u_i and u_i', and a pair of stress fields T_{ij} and T_{ij}' defined over a domain $\mathcal{V}$ bounded by a surface $\mathcal{S}$ with normal n_i. Now suppose that that both u_i and T_{ij}, and u_i' and T_{ij}' are both solutions to the Stokes equations with a point source term (equations 29 and 30). The Lorentz reciprocal theorem then states that (Kim and Karrila, 2005)

$$\oint_{\mathcal{S}} n_j(\boldsymbol{x}') T_{ij}'(\boldsymbol{x}') \hat{u}_i(\boldsymbol{\xi}) d\boldsymbol{x}'^2 - \oint_{\mathcal{V}} [\partial_j' T_{ij}'(\boldsymbol{x}')] \hat{u}_i(\boldsymbol{\xi}) d\boldsymbol{x}'^3 = \oint_{\mathcal{S}} n_j(\boldsymbol{x}') \hat{T}_{ij}(\boldsymbol{\xi}) u_i'(\boldsymbol{x}') d\boldsymbol{x}'^2$$
$$-\oint_{\mathcal{V}} [\partial_j' \hat{T}_{ij}(\boldsymbol{\xi})] u_i'(\boldsymbol{x}') d\boldsymbol{x}'^3. \tag{124}$$

Our definition of the theorem has defined the integrals in the sense of the Cauchy Principle Value (CPV) (appendix D) to allow for the case that one or more of the fields may be singular at some point in the domain (as in the case of Greens functions). For the case that

all of the fields are regular, then the CPV integral just evaluates to the regular integral. In the proof of equation 124 given by Kim and Karrila (2005) it is straightforward to extend their result to ours just by taking care when defining the integrals.

D   Cauchy Principle Value

Consider a function $f(x)$ such that $f(x \to x_0) \to \infty$. Hence we need to take care when defining an integral of $f(x)$ over a range which contains x_0. We denote the Cauchy Principle Value of an integral with a horizontal line through the integral sign, and for a singularity at the point x_0 it is defined such that (Boas, 1983)

$$\fint_a^b f(x)\mathrm{d}x = \lim_{\epsilon \to 0} \left(\int_a^{x_0 - \epsilon} f(x)\mathrm{d}x + \int_{x_0 + \epsilon}^b f(x)\mathrm{d}x \right) \tag{125}$$

This can be readily extended to higher dimensional integrals by performing the integration everywhere except in a small region around the singular point, and then finding the limiting value of the integral as the size of that region tends to zero. Also, for the case that the function is actually regular throughout this region, then the CPV equates to the standard integral.

E   Divergence Theorem

The divergence theorem states that for a volume $\mathcal{V}$ bounded by a surface $\mathcal{S}$ with outward normal n_i, then for a continuous and differentiable vector field a_i (Riley et al., 2006)

$$\int_{\mathcal{V}} \partial_i a_i \mathrm{d}\mathcal{V} = \oint_{\mathcal{S}} a_i n_i \mathrm{d}\mathcal{S}. \tag{126}$$

F   Elliptic Integrals

The complete elliptic integrals of the first and second kind are defined as (Abramowitz and Stegun, 1972)

$$K(k^2) = \int_0^{\pi/2} \frac{\mathrm{d}\theta}{(1 - k^2 \sin^2 \theta)^{1/2}}, \quad 0 \le k^2 < 1, \tag{127}$$

and

$$E(k^2) = \int_0^{\pi/2} (1 - k^2 \sin^2 \theta)^{1/2} \mathrm{d}\theta, \quad 0 \le k^2 < 1, \tag{128}$$

where k^2 is termed the modulus of the integral. Polynomial approximations can be found to evaluate the integrals (Roumeliotis, 2000) and we use the following expressions from Abramowitz and Stegun (1972):

$$K(k^2) = \sum_{i=0}^{4} a_i (1 - k^2)^i + \ln\left(\frac{1}{1 - k^2}\right) \sum_{i=0}^{4} b_i (1 - k^2)^i, \tag{129}$$

$$E(k^2) = 1 + \sum_{i=1}^{4} a_i'(1 - k^2)^i + \ln\left(\frac{1}{1 - k^2}\right) \sum_{i=1}^{4} b_i'(1 - k^2)^i \tag{130}$$

The values of the coefficients in the expansion are in table 3.

G   Components of **A**, **B** and **C**

Here we present expressions for the components of **A**, **B** and **C** in terms of complete elliptic integrals of the first and second kind (appendix F). The expressions for **A** and **B** are from Graziani (1989) although our notation is more similar to that of Manga (1994). As far as the authors are aware, equivalent expressions for **C** have never been published before, although they were undoubtedly used in the models of Lee and Leal (1982), Geller

Table 3:   The coefficients for equations 129 and 130.

a_0	1.38629436112	b_0	0.5
a_1	0.09666344259	b_1	0.12498593597
a_2	0.03590092383	b_2	0.06880248576
a_3	0.03742563713	b_3	0.03328355346
a_4	0.01451196212	b_4	0.00441787012
a_1'	0.44325141463	b_1'	0.24998368310
a_2'	0.06260601220	b_2'	0.09200180037
a_3'	0.04757383546	b_3'	0.04069697526
a_4'	0.01736506451	b_4'	0.00526449639

et al. (1985), Manga and Stone (1995) and Roumeliotis (2000). The quantities α and β are defined as (Manga, 1994)

$$\alpha^2 = x_r^2 + y_r^2 + (x_z - y_z)^2, \tag{131}$$

and

$$\beta^2 = 2x_r y_r. \tag{132}$$

K and E are complete elliptic integrals of the first and second kind respectively and they all take $k^2 = 2\beta^2/(\alpha^2 + \beta^2)$ as their modulus.

The components of **A** are:

$$A_{11} = (c_1 n_r + c_2 n_z)K(k^2) + (c_3 n_r + c_4 n_z)E(k^2), \tag{133}$$

$$A_{12} = (c_2 n_r + c_6 n_z)K(k^2) + (c_4 n_r + c_8 n_z)E(k^2), \tag{134}$$

$$A_{21} = (c_9 n_r + c_{10} n_z) K(k^2) + (c_{11} n_r + c_{12} n_z) E(k^2), \tag{135}$$

and

$$A_{22} = (c_{10} n_r + c_{14} n_z) K(k^2) + (c_{12} n_r + c_{16} n_z) E(k^2). \tag{136}$$

The coefficients c_i are given as

$$c_1 = \frac{(1-\lambda)[x_r \alpha_2 (4\alpha^4 - 18 x_r^2 y_r^2) - x_r(2y_r^2 + x_r^2)(2\alpha^4 - 3\beta^4) - y_r \alpha^2 \beta^2(y_r^2 + 2x_r^2) + x_r y_r^2 \beta^4]}{\pi(\alpha^2 + \beta^2)^{3/2}(\alpha^2 - \beta^2)\beta^4},$$

$$\tag{137}$$

$$c_2 = \frac{(1-\lambda)(x_z - y_z)[2\alpha^4 - 2\beta^4 - \alpha^2(x_z - y_z)^2]}{\pi(\alpha^2 + \beta^2)^{3/2}(\alpha^2 - \beta^2)\beta^2}, \tag{138}$$

$$c_3 = \frac{1-\lambda}{\pi(\alpha^2 + \beta^2)^{3/2}(\alpha^2 - \beta^2)^2 \beta^4} \left(\frac{x_r(-8\alpha^8 + 15\alpha^4 \beta^4 - 3\beta^8)}{2} \right.$$
$$\left. -2x_r \alpha^2(2y_r^2 + x_r^2)(-\alpha^4 + 3\beta^4) + y_r \beta^2(y_r^2 + 2x_r^2)(\alpha^4 + 3\beta^4) - 4x_r y_r^2 \alpha^2 \beta^4 \right), \tag{139}$$

$$c_4 = \frac{-(1-\lambda)(x_z - y_z)}{\pi(\alpha^2 + \beta^2)^{3/2}(\alpha^2 - \beta^2)^2 \beta^2} \left(\alpha^4(\alpha^4 - 5\beta^4) + [\alpha^2 - (x_z - y_z)^2](\alpha^4 + 3\beta^4) \right), \tag{140}$$

$$c_6 = \frac{(1-\lambda)(x_z - y_z)^2(2x_r^2 - \alpha^2)}{2\pi(\alpha^2 + \beta^2)^{3/2}(\alpha^2 - \beta^2)x_r}, \tag{141}$$

$$c_8 = \frac{(1-\lambda)(x_z - y_z)^2(\alpha^4 + 3\beta^4 - 8x_r^2 \alpha^2)}{2\pi(\alpha^2 + \beta^2)^{3/2}(\alpha^2 - \beta^2)^2 x_r}, \tag{142}$$

$$c_9 = \frac{(1-\lambda)(x_z - y_z)(-2\alpha^4 + 3\beta^4 - 4y_r^2 \alpha^2 + 4y_r^4)}{4\pi(\alpha^2 + \beta^2)^{3/2}(\alpha^2 - \beta^2)y_r}, \tag{143}$$

$$c_{10} = \frac{(1-\lambda)(x_z - y_z)^2(\alpha^2 - 2y_r^2)}{2\pi(\alpha^2 + \beta^2)^{3/2}(\alpha^2 - \beta^2)y_r}, \tag{144}$$

$$c_{11} = \frac{(1-\lambda)(x_z - y_z)(\alpha^6 - 3\alpha^2\beta^4 + 2y_r^2\alpha^4 + 6y_r^2\beta^4 - 8y_r^4\alpha^2)}{2\pi(\alpha^2 + \beta^2)^{3/2}(\alpha^2 - \beta^2)^2 y_r^2}, \tag{145}$$

$$c_{12} = \frac{(1-\lambda)(x_z - y_z)^2(8y_r^2\alpha^2 - \alpha^4 - 3\beta^4)}{2\pi(\alpha^2 + \beta^2)^{3/2}(\alpha^2 - \beta^2)y_r}, \tag{146}$$

$$c_{14} = \frac{(1-\lambda)(x_z - y_z)^3}{\pi(\alpha^2 + \beta^2)^{3/2}(\alpha^2 - \beta^2)}, \tag{147}$$

and

$$c_{16} = \frac{-4(1-\lambda)(x_z - y_z)^3\alpha^2}{\pi(\alpha^2 + \beta^2)^{3/2}(\alpha^2 + \beta^2)^2}. \tag{148}$$

The components of **B** are:

$$B_{11} = \frac{1}{2\pi\beta^2(\alpha^2 + \beta^2)^{1/2}} \left[[\alpha^2 + (x_z - y_z)^2]K - \left(\alpha^2 + \beta^2 + \frac{\alpha^2(x_z - y_z)^2}{\alpha^2 - \beta^2} \right) E \right], \tag{149}$$

$$B_{12} = \frac{x_z - y_z}{4\pi x_r(\alpha^2 + \beta^2)^{1/2}} \left(\frac{(2x_r^2 - \alpha^2)E}{\alpha^2 - \beta^2} + K \right), \tag{150}$$

$$B_{21} = \frac{x_z - y_z}{4\pi y_r(\alpha^2 + \beta^2)^{1/2}} \left(\frac{(\alpha^2 - 2y_r^2)E}{\alpha^2 - \beta^2} - K \right), \tag{151}$$

and

$$B_{22} = \frac{1}{2\pi(\alpha^2 + \beta^2)^{1/2}} \left(K + \frac{(x_z - y_z)^2 E}{\alpha^2 - \beta^2} \right). \tag{152}$$

The components of $\boldsymbol{C}$ are:

$$C_1 = \frac{9(\partial'_j n_j - y_z \text{Bo})}{4\pi D\text{Bo}(\alpha^2 + \beta^2)^{1/2}} \left[\left([\alpha^2 + (x_z - y_z)^2] n_r + y_r(x_z - y_z) \right) K \right.$$
$$\left. + \frac{E}{\alpha^2 - \beta^2} \left(n_r[\beta^4 - \alpha^2(\alpha^2 + (x_z - y_z)^2)] + n_z(x_z - y_z)(x_r\beta^2 - y_r\alpha^2) \right) \right], \tag{153}$$

and

$$C_2 = \frac{9(\partial'_j n_j - y_z \text{Bo})}{4\pi D\text{Bo}(\alpha^2 + \beta^2)^{1/2}} \left([\beta^2 n_z - x_r(x_z - y_z)n_r]K \right.$$
$$\left. + \frac{[n_r(x_r\alpha^2 - y_r\beta^2) + (x_z - y_z)\beta^2 n_z](x_z - y_z)E}{\alpha^2 - \beta^2} \right). \tag{154}$$

G.1   Special case: $x_r = 0$

For the special case that the point $\boldsymbol{x'}$ is on the axis of symmetry ($x_r = 0$) then expressions can be found for the components of $\boldsymbol{A}$, $\boldsymbol{B}$ and $\boldsymbol{C}$ that don't depend on elliptic integrals. Hence, in this scenario the components can be evaluated exactly and don't need to be approximated by polynomials. In this case the components of $\boldsymbol{A}$ are

$$A_{11} = A_{12} = 0, \tag{155}$$

$$A_{21} = \frac{3(1 - \lambda)(x_z - y_z)y_r[(x_z - y_z)n_z - y_r n_r]}{2\alpha^5}, \tag{156}$$

and

$$A_{22} = \frac{3(1 - \lambda)(x_z - y_z)^2[y_r n_r - (x_z - y_z)n_z]}{2\alpha^5}. \tag{157}$$

The components of $\boldsymbol{B}$ are

$$B_{11} = B_{12} = 0, \tag{158}$$

$$B_{21} = \frac{-(x_z - y_z)y_r}{4\alpha^3}, \tag{159}$$

and

$$B_{22} = \frac{1}{4\alpha}\left(1 + \frac{(x_z - y_z)^2}{\alpha^2}\right). \tag{160}$$

Finally the components of $\boldsymbol{C}$ are

$$C_1 = 0, \tag{161}$$

and

$$C_2 = \frac{9(\partial_i' n_i - \mathrm{Bo} y_z)}{8D\mathrm{Bo}\alpha}\left(1 + \frac{(x_z - y_z)^2}{\alpha^2}\right). \tag{162}$$

References

Milton Abramowitz and Irene A. Stegun. *Handbook of Mathematical Functions*. Dover, tenth edition, 1972.

G. K. Batchelor. *An Introduction to Fluid Dynamics*. Cambridge University Press, first edition, 1967.

M. L. Boas. *Mathematical methods in the physical sciences*. Wiley, second edition, 1983.

J.U. Brackbill, D.B. Kothe, and C. Zemach. A Continuum Method for Modeling Surface Tension. *Journal of Computational Physics*, 100:334 – 354, 1992.

E. B. V. Dussan. The moving contact line: the slip boundary condition. *Journal of Fluid Mechanics*, 77:665–684, 1976.

Charles P. Frahm. Some novel delta-function identities. *Americal Journal of Physics*, 51: 826–829, 1982.

Mark Galassi, Jim Davies, James Theiler, Brian Gough, Gerard Jungman, Patrick Alken, Michael Booth, and Fabrice Rossi. *GNU Scientific Library Reference Manual*. Network Theory Ltd., third edition, 2009.

G. Galilei. *Discourse on bodies in water*. William Leybourn, second edition, 1663.

A. S. Geller, S. H. Lee, and L. G. Leal. The creeping motion of a spherical particle normal to a deformable interface. *Journal of Fluid Mechanics*, 169:27–69, 1985.

J. Willard Gibbs. On the Equilibrium of Heterogeneous Substances. Part II. *Transactions of the Connecticut Academy of Arts and Sciences*, 3:343–524, 1878.

G. Graziani. A boundary integral equation method for axisymmetric viscous flows. *International Journal of Engineering Science*, 27:855–864, 1989.

N. M. Gunter. *Potential Theory and Its Applications to Basic Problems of Mathematical Physics*. Frederick Ungar Publishing Company, first edition, 1967.

J. Happel and H. Brenner. *Low Reynolds number hydrodynamics*. Noordhoff International Publishing, second edition, 1973.

S. Hartland. The Approach of a Rigid Sphere to a Deformable Liquid/Liquid Interface. *Journal of Colloid and Interface Science*, 26:383–394, 1968.

John David Jackson. *Classical electrodynamics*. Wiley, 3rd edition, 1999.

A. F. Jones and S. D. R. Wilson. The film drainage problem in droplet coalescence. *Journal of Fluid Mechanics*, 87:263–288, 1978.

Joseph B. Keller. Surface tension force on a partly submerged body. *Physics of Fluids*, 10:3009–3010, 1998.

Sangtae Kim and Seppo J. Karrila. *Microhydrodynamics: Principles and Selected Applications.* Dover Publications, second edition, 2005.

O. A. Ladyzhenskaya. *The Mathematical Theory of Viscous Incompressible Flow.* Gordon and Breach, first edition, 1963.

S. H. Lee and L. G. Leal. The Motion of a Sphere in the Presence of a Deformable Interface II. A Numerical Study of the Translation of a Sphere Normal to an Interface. *Journal of Colloid and Interface Science*, 87:81–106, 1982.

Michael Manga. *The motion of deformable drops and bubbles at low Reynolds number: Applications to selected problems in geology and geophysics.* PhD thesis, Harvard University, 1994.

Michael Manga and H. A. Stone. Low Reynolds number motion of bubbles, drops and rigid spheres through fluid-fluid interfaces. *Journal of Fluid Mechanics*, 287:279–298, 1995.

J. C. Maxwell. On Stresses in Rarefied Gases Arising from Inequalities in Temperature. *Philosophical Transactions of the Royal Society of London*, 170:231–256, 1879.

C. Pozrikids. *Boundary integral and singularity methods for linearized viscous flows.* Cambridge University Press, first edition, 1992.

William H. Press, Saul A. Teukolsky, William T. Vetterling, and Brian P. Flannery. *Numerical Recipes: The Art of Scientific Computing.* Cambridge University Press, third edition, 2007.

Osborne Reynolds. On the Theory of Lubrication and its Application to Mr Beauchamp Tower's Experiments, including an Experimental Determination of the Viscosity of Olive Oil. *Philosophical Transactions of the Royal Society of London*, 177:157–234, 1886.

K. F. Riley, M. P. Hobson, and S. J. Bence. *Mathematical Methods for Physics and Engineering.* Cambridge University Press, third edition, 2006.

John Roumeliotis. *A Boundary Integral Method Applied to Sokes Flow.* PhD thesis, University of New South Wales, 2000.

James Thomson. On certain curious Motions observable at the Surfaces of Wine and otherAlcoholic Liquors. *Philosophical Magazine Series 4*, 10:330–333, 1855.

Dominic Vella and Jie Li. The impulsive motion of a small cylinder at an interface. *Physics of Fluids*, 22, 2010.

Dominic Vella and Paul D. Metcalfe. Surface tension dominated impact. *Physics of Fluids*, 19, 2007.

Dominic Vella, Duck-Gyu Lee, and Ho-Young Kim. The Load Supported by Small Floating Objects. *Langmuir*, 22:5979–5981, 2006.

Dominic Joseph Robert Vella. *The Fluid Mechanics of Floating and Sinking.* PhD thesis, University of Cambridge, 2007.

Frank M. White. *Fluid Mechanics.* Mcgraw Hill, seventh edition, 1999.